NOVA SCHOOL OF SCIENCE & TECHNOLOGY

Material Science Department

André Morujo Ramos

Master of Science in

Micro and Nanotechnologies Engineering

Solution Processed NiO_x as a Hole Transporting Layer for Inverted Perovskite Solar Cells

Msc Micro and Nanotechnologies Engineering

NOVA University of Lisboa

December, 2021

Solution Processed NiO_X as a Hole Transporting Layer for Inverted Perovskite Solar Cells

André Morujo Ramos

Msc Micro and Nanotechnologies Engineering

Orientador: Dr. Manuel J. Mendes, Assistant Professor, School of Sciences and Technology – NOVA University of Lisbon

Coorientadores:

Dr. Ugur Deneb Menda, Pos-Doc Fellow, School of Sciences andTechnology – NOVA University of Lisbon

Júri:

Presidente: Prof. Rodrigo Ferrão de Paiva Martins, Full Professor, DCM, FCT- UNL.

Arguentes: Dr Fatma Pinar, , Post-Doc Researcher, Yildiz Technical University

Vogais: Prof. Manuel João de Moura Dias Mendes, Assistant Professor, CEMOP, FCT-UNL

Masters in Micro and Nanotecnology Engineering

NOVA University of Lisboa
December, 2021

Solution Processed NiO_x as a Hole Transporting Layer for Inverted Perovskite Solar Cells

"Technology is not an exogenous force over which we have no control. We are not constrained by a binary choice between "accept and live with it" and "reject and live without it". Instead, take dramatic technological change as an invitation to reflect about who we are and how we see the world."

Klaus Schwab

Acknowledgements

Com mais uma etapa da minha vida académica concluida não poderia deixar de agradecer a algumas pessoas que me ajudaram ao longo deste percurso.

Para começar gostaria de agradecer ao Prof. Dr. Rodrigo Martins e à Prof. Dra. Elvira Fortunato por nos proporcionarem todas as condições para realizar as dissertações de mestrado. Isto inclui todas as instalações (CENIMAT e CEMOP) e equipamento disponível para os estudantes da faculdade e principalmente aos alunos do departamento de Ciências dos Materiais.

De seguida quero agradecer aos meus orientadores Prof. Manuel Mendes e Dra. Deneb Menda, pela oportunidade de trabalhar numa área tão relevante e atual como a tecnologia fotovoltaica. Um agradecimento também por terem proporcionado um ambiente de aprendizagem e partilha de toda a sua experiência e conhecimento na área.

Most important, I must give a special note of thanks to Dra. Deneb Menda for teaching me everything I know on how to work in a laboratory, for all the training, even before the thesis begun and specially for always being available when needed. I also wanted to let you know that it was a privilege to work by your side and absorb your knowledge. Thank you for being the best teacher I could ask for.

Gostaria de agradecer também a todas as pessoas, investigadores e professores, do CENIMAT e do CEMOP que me auxiliaram na realização desta tese. Com especial atenção a todos os que me ajudaram no trabalho em laboratório e nas caracterizações que foram necessárias, são esses: Alexandra Gonçalves, Tomás Calmeiro, Tiago Mateus, Daniela Gomes.

Por fim não poderia deixar de agradecer aos meus pais por sempre apostarem e investirem na minha formação académica e à restante família que me apoiou ao longo destes anos. Principalmente à minha querida namorada Beatriz por estar sempre ao meu lado nos bons e maus momentos e por nunca me deixar pensar que uma ideia, sonho ou tarefa é grande demais para mim.

Também gostaria de agradecer ao meu grupo de amigos mais próximo: Filipa, Guilherme, Beatriz, Maria, Diogo e André por sempre me ouvirem quando era preciso e por estarem sempre do meu lado.

Abstract

The present thesis aims to contribute to fight the well known environmental emergency that our society is facing. To do so, this work has developed an emerging thin-film photovoltaic technology based in perovskite solar cells (PSCs), being mainly focused on the optimization of the hole transport layer (HTL) used as a *p*-contact of the devices. For that, in view of the promising propeties of Nickel Oxide (NiO_x) as HTL material, four different types of films have been investigated and compared: undoped NiO_x; magensium-doped NiOx; cobalt-doped NiO_x and co-doped (with both magnesium and cobalt) NiO_x. The properties of the developed NiO_x and perovskite films were assessed by several characterization tools: UV-Vis-NIR Spectrometry, Photoluminescence spectrometry, AFM, SEM and GIXRD. In addition, the perovskite layer was also analysed with optical and materials characterization methods.

The overarching performance of the developed NiO_x based HTLs was then tested in real PSC devices contructed with the layer structure: *ITO/NiO_x/Perovskite/PCBM/BCP/Ag*. The best results attained in this study correspond to a power conversion efficiency (PCE) of 9.49 %, an open circuit voltage (V_{OC}) of 0.87 V, a fill factor (FF) of 0.57 and short-circuit current density (J_{SC}) of 19.11 mA/cm^2, obtained by a light soaked PSC with a cobalt-doped NiO_x HTL. This is chiefly attributed to the less radiative recombination of the charge carriers in the perovskite layer deposited over such novel HTL material investigated in this thesis.

Keywords: Solar Electricity, Perovskite solar cells, NiO_x, hole transporting layer, magnesium/cobalt doping.

Resumo

A presente tese visa contribuir para o combate à conhecida emergência ambiental que a nossa sociedade enfrenta. Para tal, este trabalho desenvolveu uma tecnologia fotovoltaica emergente de película fina, baseada em células solares perovskite, focando-se principalmente na otimização da camada de transporte de buracos (HTL) usada como um contacto do tipo *p* dos dispositivos. Para isso, tendo em conta as propriedades promissoras do Óxido de Níquel (NiO_x) como material HTL, quatro tipos diferentes de filmes foram investigados e comparados: NiO_x não dopado, NiO_x dopado com magnésio, NiO_x dopado com cobalto e co-dopado (com magnésio e cobalto). As propriedades dos filmes desenvolvidos de NiO_x e perovskite foram avaliadas por várias ferramentas de caracterização: Espectrometria UV-Vis-NIR, Espectrometria de Fotoluminescência, AFM, SEM e GIXRD. Além disso, a camada de perovskite também foi analisada com métodos de caracterização ótica e de materiais.

O desempenho abrangente dos materiais transportadores de buracos, baseados em NiO_x, desenvolvidos foram então testados em celulas solares construidos com a estrutura: *ITO/NiO_x/Perovskite/PCBM/BCP/Ag*. Os melhores resultados obtidos neste estudo correspondem a uma eficiência de conversão de potência (PCE) de 9.49 %, uma tensão de circuito aberto (V_{OC}) de 0.87 V, um fator de forma (FF) de 0.57 e uma densidade de corrente de curto-circuito (J_{SC}) de 19.11 mA/cm^2, obtido com um dispositivo usando NiO_x dopado com cobalto como HTL. Isto é atribuído maioritariamente à menor recombinação radiativa por parte dos portadores de carga na camada perovskite depositada sobre o material HTL investigado durante esta tese.

Palavras-chave: Eletricidade Solar, Células Solares de Perovskite, NiOx, camada de transporte de buracos, doping de magnésio/cobalto**.**

Contents

List of Figures

List of Tables

Symbols

µm - Micrometer

A - Amperes

cm – Centimeter

eV - Electronvolt

mA - Miliampere

mg - Miligram

min. - Minute

mL - Mililiter

mm - Millimeter

N/m – Newton/metre

nm - Nanometer

ºC - Degrees Celsius

Pm-picometer

rpm - Rotations per minute

s - Second

V -Volts

W - Watts

λ - Wavelength

Ω - Ohms

Acronyms and Abbreviations

Ag - Silver

AMX_3 - Perovskite Structure

AFM - Atomic force microscopy

BCP - Bathocuproine

CB - Conduction Band

Co:NiO_x- Cobalt doped Nickel oxide

DSSC - Dye-sensitized solar cell

DMF- Dimethylformamide

DMSO-Dimethyl sulfoxide

E_g - Bandgap

EIS- Electrochemical impedance spectroscopy

ETL - Electron transport layer

EtOH - Absolute Ethanol

FF - Fill factor

FIB - Focused ion beam

FTO - Fluorine-doped Tin Oxide

GBL - Gamma-Butyrolactone

GDP- Gross Domestic Product

GIXRD - Grazing incidence X-ray diffraction

HTL - Hole transport layer

HTM - Hole transport material

HOMO- Highest Occupied Molecular Orbital

IPA - Isopropanol Alcohol

ITO - Indium-doped Tin Oxide IZO - Indium-doped Zinc Oxide

J_{sc} - Short-Circuit Current Density

MAI - Methylammonium Iodide

$MAPbI_3$ - Methylammonium Lead Iodide

Mg:NiO_x- Magnesium doped Nickel oxide

MgCo:NiO_x- Magnesium and Cobalt doped Nickel oxide

Ni- Nickel

NiO - Stoichiometric nickel oxide

NiO_x - Non-stoichiometric nickel oxide

NIR - Near infrared

Pb - Lead

PbI_2 - Lead iodide

PCBM - [6,6]-Phenyl-C61-butyric acid methyl ester

PCE - Power Conversion Efficiency

PEDOT: PSS - Poly(3,4-ethylenedioxythiophene):polystyrene sulfonate

PSC - Perovskite solar cell

RMS - Root mean square

RT - Room temperature

SEM - Scanning electron microscopy

Spiro-MeOTAD - 2,2',7,7'-tetrakis(N,N-di-p-meth-oxyphenylamine)-9',9'-spirobifluorene

T - Transmittance

UPS - Ultraviolet photoelectron spectroscopy

UV-Vis - Ultraviolet-Visible

VB - Valence Band

V_{OC} - Open-circuit voltage

WF- Work function

XPS - X-ray photoelectron spectroscopy

XRD - X-ray diffraction

Motivation and Objectives

During the present global pandemic scenario we have learnt that our planet is fragile, and COVID-19 made us even more aware of climate emergency and the fragility of our society. The 2019 Intergovernmental Panel on Climate Change reports argued that we only have ten years left until climate change becomes irreversible. This problem is a direct result of a fossil fuel driven economy. For example, in 2019, the subsidies for fossil fuel companies were estimated to be 55 billion euros a year, and 56% of the COVID-19 recovery funding allocated to energy companies is being attributed to fossil fuel problems by G20 governments. This shows, not only, that fossil fuel consumption is growing at a greater pace, compared with renewable energy, but also that the investment in technologies related to renewable sources of energy is being underfunded. As countries aim to increase their GDP to have exponential growth, it is expected that the energy consumption increases accordingly. This shareholder capitalism model with short-term and narrow view of growth does not act towards an environmental stable society. A new economic model, based on a stakeholder perspective, with long-term growth goals in sight, is now mandatory to tackle this crisis. This idea of stakeholder capitalism was first introduced in the first *Davos Manifesto* in 1973 and has been updated till today[1]. This *manifesto* gives a guideline with a set of ethical principles that uphold a value creation not only for the shareholders but also for the stakeholders - employees, customers, suppliers, local communities, and society at large. One of the ways for policy intervention towards a more sustainable growth is investment in technology and incentives for green R&D, such as photovoltaic technology, since non-renewable resources still represent over 80% of global energy consumption. If we cannot find alternatives to meet the global demand for energy, we will face inevitably an increase in production costs, a productivity decline and serious climate change.

Although the fossil fuel industry still represents the major source of energy, some countries have been investing in electricity production from renewable resources, such as photovoltaic technology.[2]

My hope and ultimate objective for this thesis is to contribute to overcome technical limitations by helping push the envelope in the photovoltaic field. In order to accomplish this, PSCs present an adequate proposition, since they show increasing power conversion efficiency (PCE), that rivalize the performance of comercial crystaline silicon solar cells, while making use of low cost materials with simple fabrication process. This work aims to optimize the perovskite absorber layer and HTL using doped NiO_x in thin films in the inverted *p-i-n* architecture of PSCs. NiO_x processing is already considered a mature technology and its integration in PSCs shows good widely reported results in literature. This compound therefore presents a promising alternative to the standard hole selective contacts as: Spiro-OMeTAD, PEDOT – PSS and PTAA. Such organic compounds exhibit critical issues regarding stability and high cost, which is were inorganic materials, particularly NiO_x, have a clear advantage, given that they are low cost, have better stability and can be processed at higher temperatures. Another possibilty offered by NiO_x is the chance to be doped, this allows the conductivity and energy levels to be modified, which results in an overall improvement in performance enabling adaptation to work with different perovskite materials. The method chosen to deposit this HTL material on the ITO surface was spin-coating, since it is a simple and cost effective process that shows good film uniformity.

1. Introduction

Sunlight is the most abundant natural resource known to mankind, with an enormous amount of energy being delivered of $3x10^{24}$ J per year[3]. It is safe to collect and benefits from a cleaner way to produce electricity in order to keep a sustainable economic growth, so it is only logic that in the upcoming years photovoltaic technology continues to expand, as we can visualize in the Figure 1. This propels the search for compact and more environmentally friendly ways of converting and harvesting energy. Perovskite solar cells have already proven their high efficiency[4] and are now considered one of the most promising technologies in research, in this field[5].

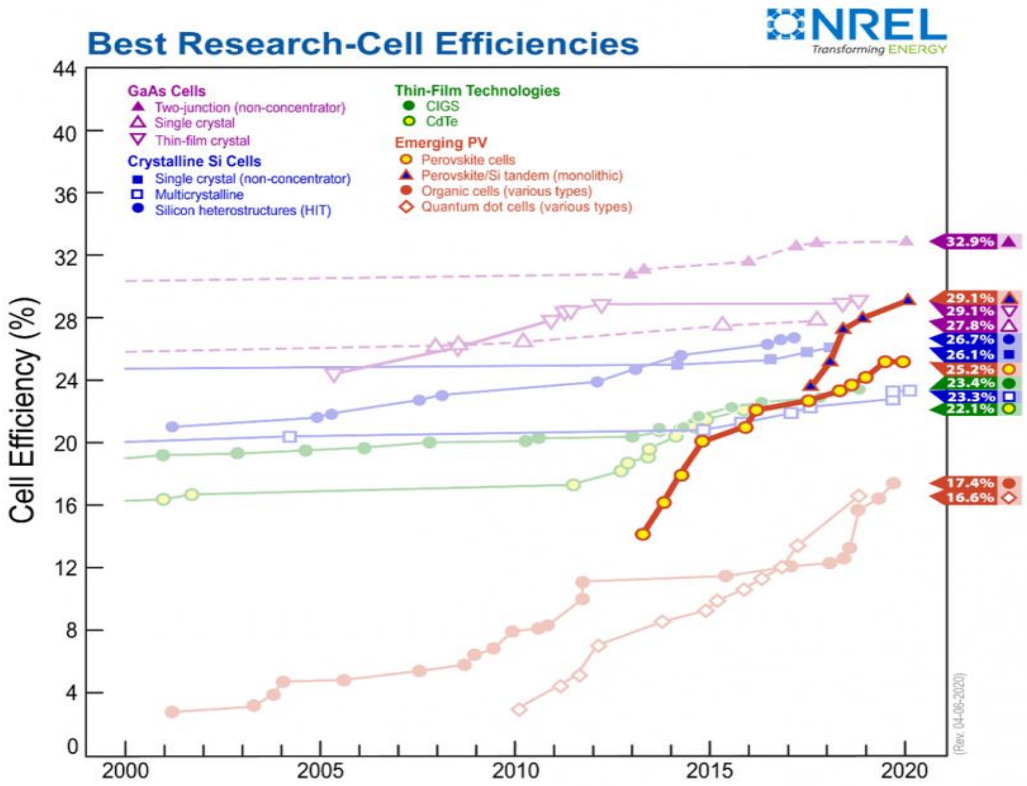

Figure 1- Graph showing the evolution of record efficiency of PSC technology during the past decades, extracted from the latest NREL efficiency chart for all PV technologies[5]

1.1. Perovskite

1.1.1. Historical remarks

The term '*perovskite*' first appeared around 1839, when a sample of *calcium titanate* ($CaTiO_3$) was coined in Ural Mountains in Russia. It was then transferred from Saint Petersburg to Berlin by the Russian mineralogist Alexander Kämmerer to German crystallographer and mineralogist Gustav Rose. In Berlin it was analysed in more depth. After Rose accessed its properties, he named the crystal after the Russian politician and mineralogist Lev Perovski.[6]

However, today this term is used to refer to ionic compounds with the general formula of AMX_3. Perovskites can be split in two kinds: perovskite inorganic oxides or halides perovskites. The halides can be divided in alkaline

perovskites or organometallic perovskites[7]. The general chemical formula for pure perovskite compounds is AMX_3, represented in Figure 30 (Appendix section H).

One of the most attractive perovskite absorbers is an organo-lead halide-methylammonium lead - $CH_3NH_3PbX_3$ where X represents a halogen element such as I^- (iodine). These hybrid perovskites seem to be an appealing proposition since it can be synthetized in a base solution at low temperature, such as sol-gel synthesis, which simplifies the fabrication process while offering a strong optical absorption, high charge mobilities, that are important factors to take in account when developing a solar cell[7]. PSCs using methylammonium lead iodide, $CH_3NH_3PbI_3$, have been highly researched and already shown optimistic results as they exhibit high conversion efficiency (>25.6%)[2,8], although there are still some significant stability issues with it.

1.2. Architecture of perovskite solar cells

There are many types of devices and different structures that this kind of solar cells can have. Two of the most used architectures for perovskites are conventional *n-i-p*, which we can see in Figure 2 a) and b), and the other one is inverted structure, as shown in Figure 2 c) and d).

1.2.1. Conventional n-i-p Structure: Glass/TCO/ETL/Perovskite/HTL/Metal

This kind of architecture, particularly the mesoscopic *n-i-p*, is the original structure of PSCs and one that is still used. It consists of a glass substrate coated with a TCO cathode , usually ITO or FTO, with a thick mesoporous metal oxide layer of an ETM (electron transport material), for mesoscopic *n-i-p*, and a compact metal oxide layer for *n-i-p* structure. This film is responsible for conducting the electrons generated in the active perovskite layer and is made of a *n*-type semiconductor. The next layer is the perovskite layer, acts as the device absorber, followed by the HTL, which is the hole conductor layer of the device. Spiro-OMeTAD[9] is one of the most common HTM used in the literature. – ETL/HTL acts as a selective carrier extraction channel. The device fabrication ends with a deposition of a metal acting has the top electrode, and usually this layer has between 100 and 150 nm of thickness[2,10,11]. Although devices based on *n-i-p* heterojunction exhibit good performance figures, Xing et al.[12] found out that the diffusion length of holes is slightly shorter than that of electron due to a larger effective mass of hole, therefore *p-i-n* planar architectures began to be explored in this field.

1.2.2. Inverted p-i-n Structure- glass/TCO/HTL/perovskite/ETL/metal

When the first layer to be deposited is the HTL on the back contact/substrate, the device is fabricated in inverted *p-i-n* configuration, and one of the most common *p*-type semi-conductors used to this purpose is poly(3,4-ethylenedioxythiophene) poly(styrene-sulfonate) (PEDOT-PSS). Recently, the efficiency of this architecture has improved, the most efficient PSC based *p-i-n* structures employ contrivable molecules with controlled EA (enviromental ambient) processed at low temperature (≈100 °C) to tailor the conductivity and energy level of the NiO_x HTL, which makes a device with 22.13% PCE[11,13].

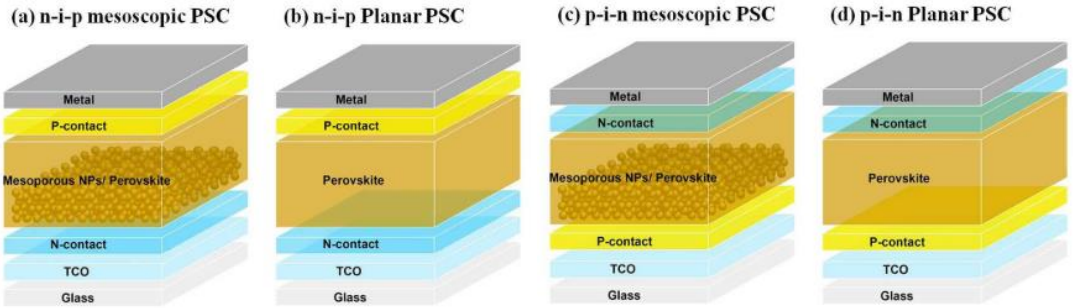

Figure 2 - Device structure of a) n-i-p mesoscopic,b) n-i-p planar,c) p-i-n mesoscopic and d) p-i-n planar PSC.[14]

1.2.3. Substrate vs Superstate configuration

There is another criteria used to categorize the configuration of PSCs which indicates from where the solar cell is illuminated, so called – substrate and superstate configuration. As it is shown in Figure 31 (Appendix section H). and the light can enter the device in one of two ways, from the front contact, in substrate configuration, or in the superstate configuration, where the substrate is first illuminated.[15]

The superstate configuration offers the challenge of finding transparent substrates to use in PSCs, usually most researchers use FTO and ITO has substrates since they have high optical transmittance and present low electrical resistivity which are key elements in PSCs devices as photoelectrodes[16,15]. Huang et al. 2016[16] even proposed, to make PSC devices more sustainable, a simple and low-temperature processes that include organic solvent washing, ultra-sonic cleaning, and UV ozone treatment to recycle FTO/glass substrates[16]. This configuration is one of the most common in today's literature since it offers, to date, the possibility of achieving more PCE out of the devices compared to substrate-configuration metal-halide perovskite solar cells (PSCs) fabricated on opaque substrates[17]. This challenge is not present when using substrate configuration since the light enters the device from the film side, this allows the use of flexible polymers[18], metals and even optically transparent wood substrates[15,19,]. This architecture allows for an easy-fabrication process while ensuring cost-effectiveness, and is known for having negligible J-V hysteresis effect[17,20,21].

1.3. Hole Transporting layer

As mentioned before, ETL/HTL act as a selective carrier extraction channel and the HTL is responsible for transporting the holes generated in the perovskite layer to the solar cell anode. This thin film prevents the direct contact between the perovskite layer and the top metal contact, which minimizes the charge recombination at the interface while also preventing degradation of the device[22]. A compatible HOMO energy level of HTM to the valence band energy (VBE) of the perovskite is key to ensure a good hole mobility[23,22].

After the photoexcitation, in the perovskite absorber layer, electrons are injected into the ETL, while holes are transferred to the HTL, these photogenerated charge carriers (electrons and holes) are collected as photocurrent at the front and back contacts of the solar cell. When this happens undesirable charge recombination might occur at the interfaces HTL/Perovskite and ETL/Perovskite[23,22] , to prevent this the chosen HTM should have a CB level higher than the perovskite. In Figure 3, a summarized energy level diagram of perovskites and charge-extraction layers is shown, which guides for material selection in PSCs.

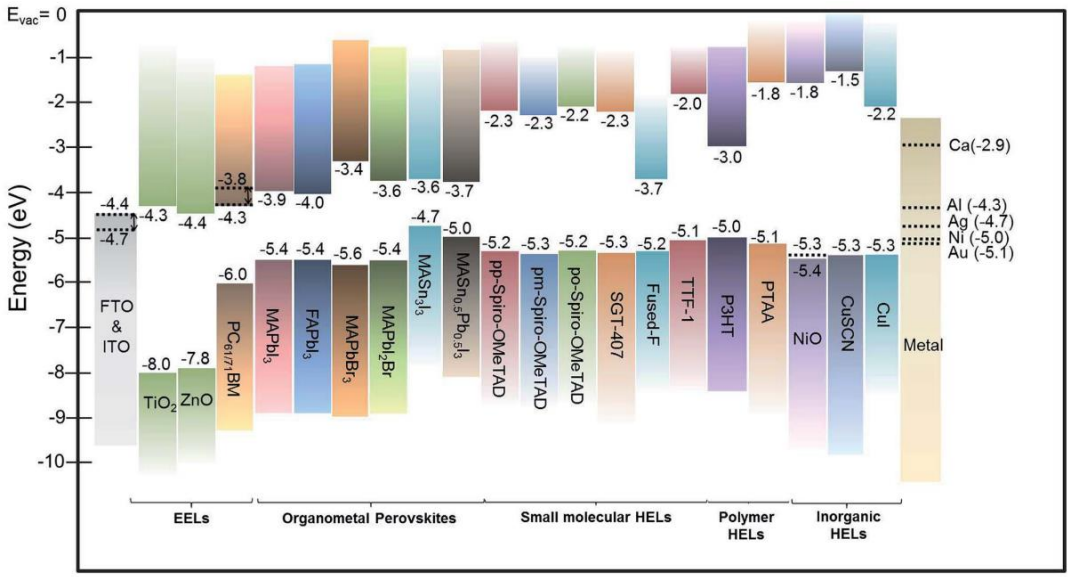

Figure 3 - A summarized energy level diagram of the representive organometal perovskites and charge-extraction interlayers. The dot lines represent the WF of the materials[24].

1.4. Nickel Oxide as HTM

One of the routes taken by many researchers is the use of NiO_x as a HTM (hole transport material), since it possesses many qualities that serve purpose to the HTL. Some of the advantages of this HTM is the favourable energy band positions, high hole mobility, superior chemical stability, and low cost manufacturing[25]. This semi-transparent *p*-type semiconducting material with wide band gap width ranging from 3.6 to 4.0 eV, deep valance band (5.6 eV), and high conduction band that helps to prevent the undesired electron leakage [26–28] . It also shows other attractive application beyond the PSCs field, since it shows electrochromic, thermoelectric properties has well as high chemical resistance [28–31].

Nickel oxide (NiO_x) has a cubic structure, with Ni (II) and O_2 sites, in its pure stoichiometric this oxide is an insulator. However due to the presence of NiOOH and Ni_2O_3 oxygen is always present in excess, this results in Ni vacancies (holes) which makes NiO_x usually a *p*-type semiconductor[32,26,27]. This metal oxide, when compared to organic HTMs presents a more stable structures which ends up being more thermally stable since it has non-corrosive properties[33,34].

1.5. NiO_x doping strategies

To extend NiO_x capabilities, various tuning strategies can take place, doping this material is one of those. Doping agents can optimize optoelectronic properties of NiO_x by modifying its work function, enhancing conductivity, improving of the hole extraction from perovskite, while decreasing recombination at that interface, which may, in some cases, be correlated with a better crystallinity in the perovskite layer caused by doped NiO_x underneath. All these changes are accountable to the enhance performance figures already reported in the literature[26,34,35].

The *p*-type nature of NiO, which is an insulator in its stoichiometric form, is due to its Ni^{2+} vacancy. This mechanism is well described by equation (1) and (2):

$$\frac{1}{2}O_2 \rightarrow O_0^x + V_{Ni}'' + 2Ni_{Ni} \quad (1)$$

$$Ni_{Ni} \rightarrow Ni^x_{Ni} + h \quad (2)$$

The negative charge in the nickel vacancy is then compensated by Ni^{3+} oxidation state and Ni_{Ni} (from equations above) acts as an shallow acceptor level. The doping successfully happens when there is a substitutional replacement of Ni^{2+} with a cation with a lower oxidation state or by modifying the oxidation state (non-stoichiometry) of the film[32,34]. The *p*-type nature of NiO_x is related to the NiOOH and Ni_2O_3 states in the structure. By altering the concentration of Ni or oxygen vacancies one can modify its fundamental properties such as work function, electrical conductivity and hole concentration. This last one is linked to the trivalent states (Ni_2O_3) thus excess oxygen[27]. Even though a higher Ni^{3+}/Ni^{2+} ratio is expected to result in increased hole concentration it may also result in limited electrical conductivity. By altering Ni vacancies/holes, which can happen through doping, we can improve the hole conductivity without a drop in electrical conductivity of NiO_x[27].

Since doping in NiO_x is already widely studied, several strategies can be found in the literature, such as: passivation layers, chemical and elemental doping [32,36–39], molecular doping[40], capping layers, and also various surface treatments like Ultraviolet Ozone (UV-O_3) and O_2-plasma[41–43].

1.5.1. Importance of Cobalt and Magnesium doping

In the current literature there are many possibilities in terms of NiO_x doping agents, some of those options and strategies were exposed in the previous chapter. In this section some reasons for choosing cobalt and magnesium as doping materials will be explained.

Li et al. 2017[44] reports an XPS data that shows that magnesium increases the Ni^{3+}acceptors contents in $NiMgO_x$. In his work[44] it is stated that Ni^{3+}/Ni ratio rises from 39% to 49% when the Mg concentration increases from 0% to 12%. This is an indication that magnesium can positively contribute to the increase of relative content of Ni^{3+} acceptors in the $NiMgO_x$ films thus making NiO_x more conductive[44,45]. Another reason for this selection is present in Chen et al. work[45], where 15% of Mg^{2+} was used as a co - doping strategy with the Li^+ doped nickel oxide film. The magnesium content present in this layer was found to compensate the undesirable positive shift of its valence band, caused by Li^+ incorporation into the lattice[27,45], decreasing the device's V_{OC}[46,47]. This doping strategy is also possible because the mismatch of the ionic radii of Li^+ (0.76Å), Mg^{2+}(0.71Å) and Ni^{2+}(0.69Å) is quite small, conferring good lattice stability to the $Li_xMgyNi_{1-x-y}O$ ternary oxides[45]. Regarding cobalt as a doping option, many researchers[27,46,48,49] have found that the incorporation of it increased the work function of the HTL.This provides a closer band alignment to the valence band energy for the $MAPbI_3$ layer[27,48]. As previously discussed in the magnesium doping, the cobalt integration in NiO_x also increases the ratio between Ni^{3+} and Ni^{2+}, indicating the oxygen deficiency in NiO_x and thus the presence of Ni vacancy. A higher Ni^{3+} acceptors in $Co:NiO_x$ might contribute to an increase in hole conductivity[46,48–50]. This compound is also a good match with NiO since their atomic radii of cobalt and nickel are almost the same (152 pm and 149 pm. for cobalt and nickel, respectively)[48]. From EIS measurements performed by Lee et al.[48] it was found that the overall resistance of the devices and interfaces in $Co:NiO_x$ -based devices were reduced as compared to that of pristine NiO_x[46,48], leading to an increase recombination resistance. The overall performance of the devices explored in the literature were very promising with cobalt, getting efficiencies up to 17.77% [46,48,49] and magnesium also shows some exciting performance figures[27,44,45].These are the main reasons that led us to choose these two compounds as doping agents.

2. Methods and Materials

2.1. Device Preparation

2.1.1. Substrate Preparation

The device fabrication begins by cutting ITO coated glasses (2.5 x 2.5 cm), after that these substrates go through a cleaning procedure. This cleaning procedure is well documented in the appendix section B of this document. The preparation ends by setting Kapton tape with 2-3 mm of the ITO side, this allows the bottom electrode to be partially exposed after the spin coating deposition.

2.1.2. NiOx HTL deposition

For The NiO_x HTL deposition, since we are using sol-gel method to manufacture solar cells, a spin coating technique is used. The spinner (Laurell WS-400-6NPP-LITE) is programmed for one step at 1500 rpm for 30 seconds, with a volume deposit on the substrate of 150 µl, which is followed by drying on a hot plate for 20 minutes at 80 ºC. The layers are composed by 2 layers of each NiO_x solution (which are described in appendix D), so the mentioned procedure takes place twice. Finally, an annealing step takes place at 450 ºC for 1 hour, in a Nabertherm furnace. For the annealing study a tube furnace and a hot plate were also used for this stage.

2.1.3. Perovskite layer deposition

The perovskite solutions (described in the appendix section D) were deposit by spin coating technique. To obtain the perovskite layer a three step spinner program was used: 500 rpm for 1 second (500 rpm/s), followed by 1500 rpm for 1 second (1000 rpm/s) and then 4000 rpm for 40 seconds (1500 rpm/s). For the deposition 200 µl of perovskite precursor solution was dropped on the substrate and an antisolvent washing was performed by 120 µl of chlorobenzene at 25th second of the program. This washing procedure causes the removal of the solvent of the perovskite precursor and the start of crystallization on the film. After the deposition, the layer is annealed on a hot plate at 100 ºC for 15 minutes. The perovskite solution was used warm and stirred at 60ºC prior to the deposition. The NiO_x substrates go through an UV Ozone treatment for 20 min. at room temperature with 7 cm distance from the light source, and they are also pre heated at 80 ºC before the perovskite precursor solution is applied onto them.

2.1.4. ETL deposition

The ETL deposition takes place right after the perovskite layer is annealed and cooled down to room temperature. The deposition of PCBM solution (described in appendix D) was performed by spin coating at 1500 rpm for 30 seconds, with 90 µl of PCBM volume, and then dried in a hot plate at 100ºC for 5 minutes.

2.1.5. Buffer layer deposition deposition

Right after the ETL deposition, 90 µl of bathocuproine (BCP) solution (preparation described in appendix D) is drop casted to form a thin film acting has a buffer layer. The spinner is programmed at 4000 rpm for 40 seconds, after which the sample is dried for 5 minutes in a hot plate at 100ºC. Finally, after the deposition the bottom electrode area, where the Kapton tape used to be, is cleaned with absolute ethanol to expose the ITO surface.

2.1.6. Top Electrode deposition

Before the deposition of the electrode and after the BCP deposition, a mask with 8 windows with an area of 10 mm^2 are taped on the substrates to create the contacts that make the active cell area. The metal is deposit by thermal evaporation in a vacuum chamber at $P < 6 \times 10^{-6}$ mbar.

2.2. Characterization

2.2.1. SEM

The top-surface view images were examined by scanning electron microscopy (SEM) Hitachi Regulus 8220.

2.2.2. UV-Vis-NIR Spectrophotometry

The reflectance and total transmittance, of the analysed samples, were measured using Perkin Elmer Lambda 950 spectrophotometer with an ISR-260 integrating sphere, using a wavelength range of 300-900 nm and a scan speed of 382.42 nm/ min.

2.2.3. AFM

Atomic force microscope topographs were acquired with an Asylum Research MFP-3D Standalone system operated in room conditions, in alternate contact mode, using commercially available silicon probes (Olympus AC160TS, f0 = 300 kHz, k = 26 N/m). Topographs were low-level planefitted and exported to images using the Gwyddion software.

2.2.4. Opto-electronic Characterization

The J-V curves were obtained by VeraSol-2 LED Class AAA Solar Simulator from Oriel, the forward and reverse scan was applied (I_{SC} to V_{OC}) under ambient conditions at RT and AM1.5G illumination conditions ($1kW/m^2$).

2.2.5. XRD

The crystal structures characterization of the NiO_x layers was done using Grazing incidence X-ray diffraction (GIXRD) by a PANalytical X'Pert Pro X-ray diffractometer in Bragg-Brentano geometry, with a radiation source of Cu-Kα (λ=1.5406 Å) and a grazing angle of 0.4º. For the Perovskite characterization the same equipment in the same conditions was use but with no grazing angle.

2.2.6. Photoluminescence

The steady state photoluminescense (PL) data was obtained using a PerkinElmer LS 55 with an excitation at 600 nm in a range of 650 to 900 nm aided by BL Studio software.

3. Results and Discussion

3.1. HTL development and characterization

The aim of this work is to optimize the HTL contact, made from a doped or undoped NiO_x thin film, to be integrated in an inverted perovskite solar cell (PSC) architecture: *ITO/NiO_x/Perovskite/PCBM/BCP/Ag*. In view of such device structure, the HTL properties were studied by fabricating the NiO_x films via spin coating the precursor solution onto ITO coated glass substrates, being one of the goals to assess which doping agent works the best for the HTL.

For a starting point of this thesis, a series of characterizations were conducted on the 4 different NiO_x layers- pristine (undoped) NiO_x, magnesium-doped NiO_x, cobalt-doped NiO_x and co-doped magnesium and cobalt doped NiO_x.

In this section it is presented an analysis of the data obtained from UV-Vis-NIR Spectrophotometry, XRD, and AFM in the different layers of NiO_x. For each sample the deposition conditions remained the same: rotation speed, rotation time, UV-Ozone substrate pre-treatment height and time, as well as humidity and temperature conditions.

3.1.1. Effect of doping agent – Optical analysis

The first characterization conducted was an optical one, the transmittance and reflectance were measured by spectrophotometry, with the equipment described in the Methods and Materials section of this document. For that purpose, the 4 different precursor solutions were deposited on glass substrates followed by anneal step.

This data was used to obtain the bandgap value of the NiO_x for each doped layer, by an extrapolation of Tauc plot equation and the absorption coefficient, in which α represents the absorption coefficient, and it is calculated from equation (3), where T represents the transmittance (%) and d, the thickness of the film in question[51,52]. Since the films have negligible reflectance, which can be verified by looking at the plots of the reflectance in Figure 21 of the appendix E of this document, we used equation (3) that takes only transmittance into consideration[51,52]. Since the thickness of the deposited NiO_x layers were not determined by any experimental method (SEM-FIB or perfilometer) a d value of 25 nm was used for the calculations. This value is based on Choi et al. 2021 work[27], because this thesis followed their guidelines.

$$\alpha = -\frac{1}{d}\ln(T) \qquad (3)$$

$$(\alpha h\nu) = B(h\nu - Eg)^n \qquad (4)$$

The Tauc formula is based on the equation (4), where B is a constant, hν is the photon energy, E_g is the band gap energy, and n is $1/2$ or $3/2$for allowed and forbidden direct transitions, respectively. Although for this case, NiO_x, the value of n is $1/2$, after the Tauc formula is ploted, the direct bandgap (E_g) is given by the intersection of a prolongation of the linear part of the graph with the x axis of the plot[51,52].

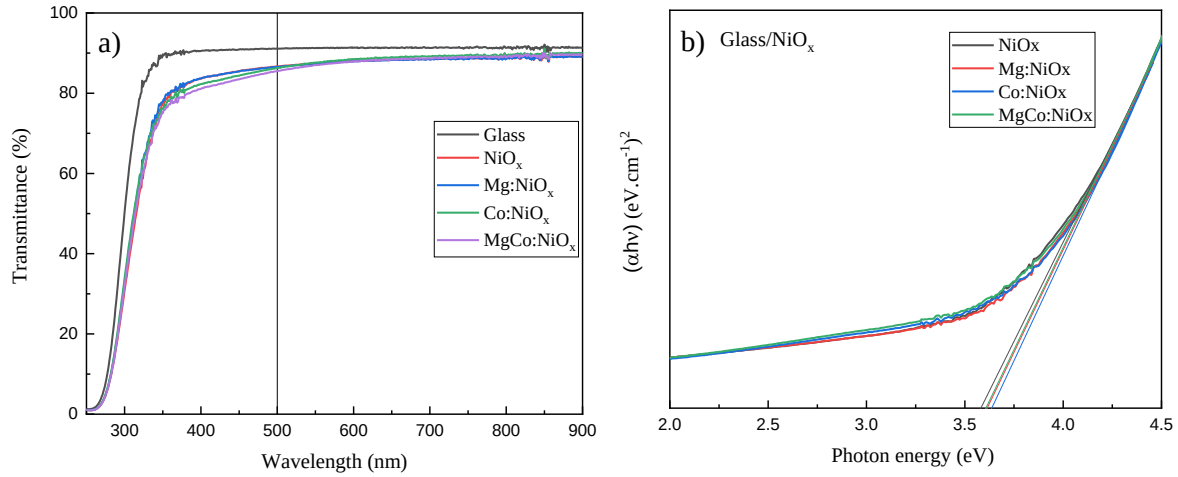

Figure 4 - a) Transmittance plot of NiO_x samples and glass. b) Tauc plots of $(\alpha h\nu)^2$ vs Photon Energy of the same transmittance measurements with the calculated bandgaps.

The obtained data, is represented in the plots in Figure 4, and it can be observed a summary of the bandap values and transmittance percentage at 500 nm for all the different NiO_x samples in Table 1. According to this data, the values of NiO_x[27,53,] are in a range of 3.58- 3.64 eV, with a difference of ΔE_g=0.06 eV. When NiO_x was doped with cobalt[27,49] the bandgap value reached its hight by 0.06 eV, 0.04 eV with magnesium[27,32,54] and when co-doped[27] it increased 0.03 eV. This bandgap change is only by a small margin, which is also relatable with the minimal difference of the transmittance data, at 500 nm, between the different samples (ΔT=1.17%). The pristine NiO_x ,cobalt-doped NiO_x and magnesium-doped NiO_x film values are in the range found in the recent literature[27,32,53,54]. However, Kaneko et al.[49] has shown a slight variation from this data, in their findings the incorporation of cobalt slightly narrowed the band gap from 3.92 eV to 3.87 eV.

Table 1- Bandgap and transmittance values for different NiOx- doped and undoped films

NiOx HTL	***Bandgap (eV)***	***Transmittance (%) at 500 nm***
Pristine NiO_x	3.58	86.69
Magnesium doped NiO_x	3.62	86.57
Cobalt doped NiO_x	3.64	86.29
Co-doped NiO_x	3.61	85.52

3.1.2. Effect of annealing equipment – Optical analysis

Since the annealing step is one of the main stages where it can cause some variability in the NiO_x thin films[36,55], its effects were studied using 3 different equipments: furnace (Nabertherm), tube furnace and a hot plate. In the appendix section I, it is presented images of the furnace, tube furnace and hot plate in Figure 32, Figure 33 and Figure 34, respectively

After measuring transmission and reflectance of the thin films we used the same extrapolation, similar to what was done in the previous subchapter, the obtained plots for each sample, using the three different equipments, are presented in Figure 5.

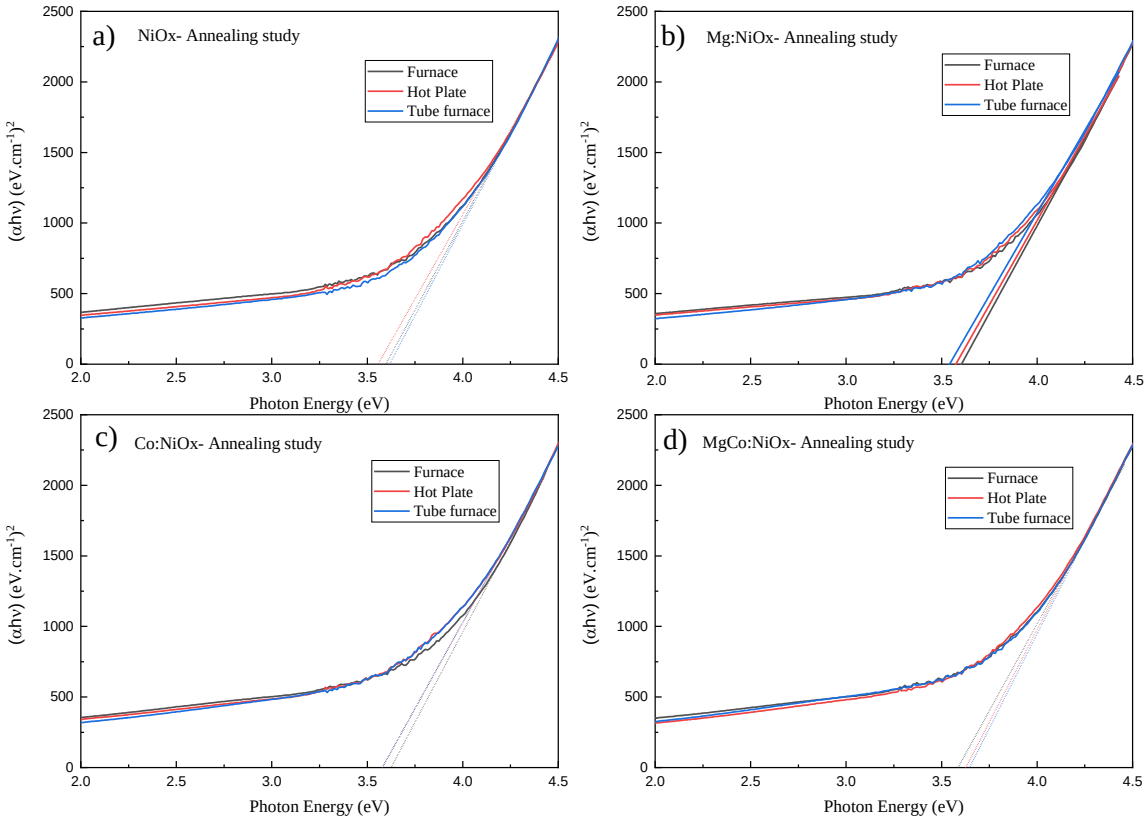

Figure 5 - Tauc plots of $(\alpha h\nu)^2$ vs Photon Energy with the calculated bandgaps, using three different annealing equipment for a) Pristine NiO_x, b) Mg:NiO_x, c) Co:NiO_x, d) MgCo:NiO_x.

By analysing the graphs in Figure 5, it is concluded that the equipment used for the annealing stage did not show major changes in the bandgap of the film. It remains in approximately the same range (3.55 eV-3.63 eV) as the previous analysis present in Figure 4. However, it shows a difference in the performance of the devices when using different annealing equipment, something that is discussed in section 3.3.1 of this document. In the appendix section E of this report, the transmittance and reflectance plots for each doped layers of NiO_x and the equipment used for annealing are presented in Figure 22 and Figure 23 respectively. It can be observed that, once again, the equipment used does not change the transmittance significantly and reflectance remains low.

From analysing the transmittance at the 500 nm mark, it appears that, apart from the co - doped NiO_x sample, the tube furnace shows the higher transmittance, followed by hot plate and furnace respectively. For the co-doped sample, the hot plate delivers the higher numbers followed by the tube furnace and furnace.

3.1.3. Surface analyses of NiO_x layers

One of the major concerns when fabricating thin film solar cells is the surface quality of each layer, and the morphology is dependent on so many factors such as: annealing conditions, precursor solution temperature and aging, additives, and deposition method[56].

To study the morphology and assess the topographical information of the different NiO_x samples, Atomic Force Microscopy (AFM) was conducted on the different NiO_x doped and undoped thin films deposited on a glass

substrate. Using Gwyddion software on the AFM images the root mean square (RMS) values of the height deviations were calculated. This number reflects the roughness of the analysed film.

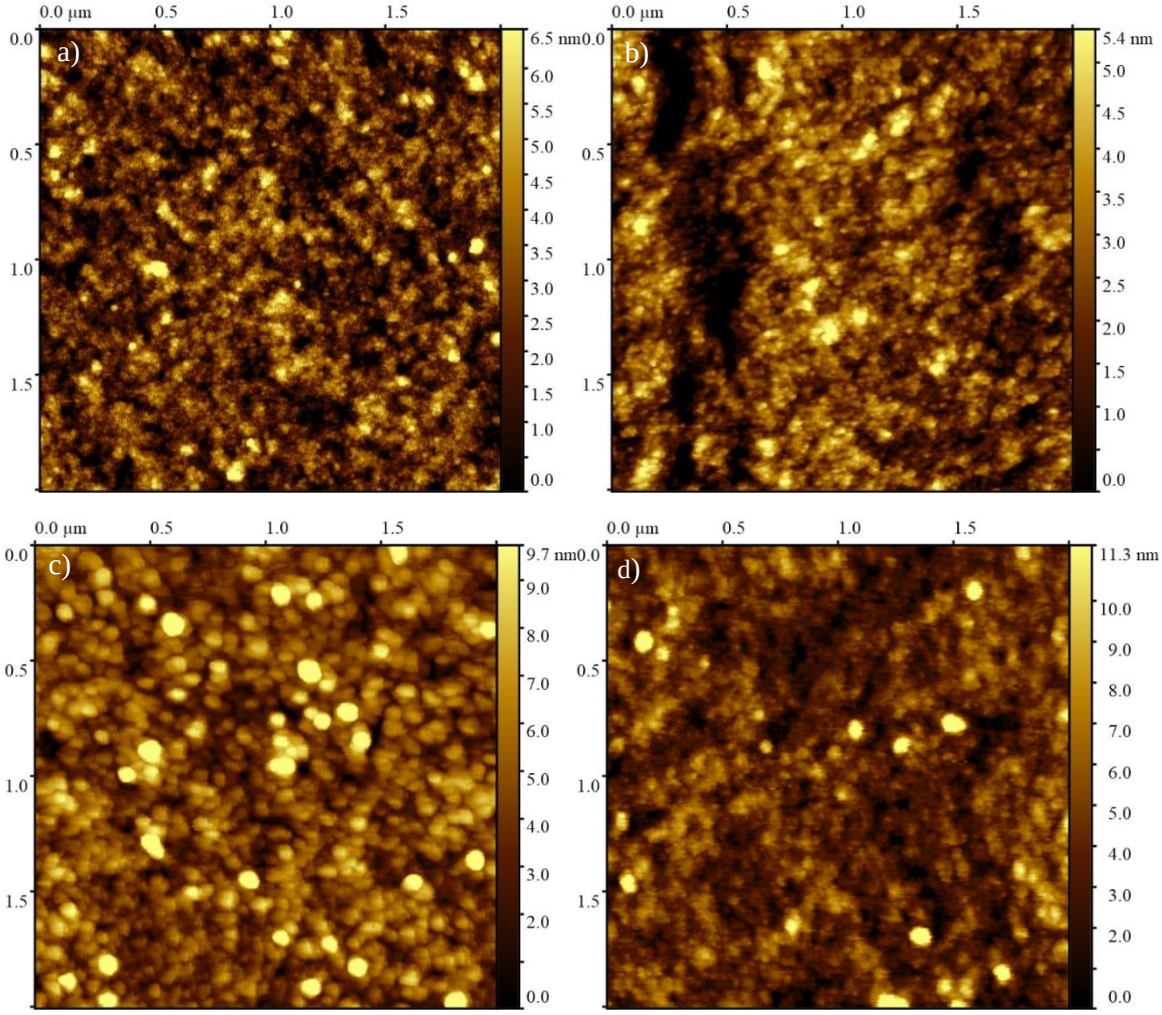

Figure 6 - AFM topographical images obtained by Gwyddion software on the different NiO_x samples. a) undoped NiO_x b) Co: NiO_x c) Mg:NiO_x d) MgCo:NiO_x.

The morphological characteristics of the NiO_x films are shown in Figure 6, and Table 2 shows the values of the RMS given by each sample. Since the films were deposited on a glass substrate for this characterization procedure, its surface was also analysed via AFM, and the value obtained was 2.728 nm (the topographical image of the glass substrate is presented in the appendix section F, Figure 24, of this document). This value, when compared to the other ones, is the highest. The decrease in the RMS value of the samples when covered by a thin film of NiO_x suggests that this layer is very thin and also that the samples cover the glass surface completely. When comparing all four samples, it can be assessed that the samples with no cobalt doping are less rough, which indicates that the cobalt doping might be responsible for an abrupt increase in the RMS value of the sample. This effect is also reported in literature: in Choi et al. work[27] cobalt revealed an increase in the NiO_x film roughness when co-doped, this time with lithium[27]. By looking at the samples with magnesium - doped NiO_x, the opposite seems to happen, those ones have the lowest RMS value, which indicates a smoother surface when compared with the pristine NiO_x film and, when co-doped with cobalt, this value seems to attenuate its effect. This finding has already been

noticed by other academics[27]. However, when the same characterization is performed on ITO and FTO, available in appendix section F (Table 9), the same pattern was not observed.

Table 2 - RMS values for different NiO_x- doped and undoped films

NiOx Sample	***Average RMS (nm)***
Pristine NiO_x	1.447
Magnesium doped NiO_x	1.263
Cobalt doped NiO_x	2.080
Co-doped NiO_x	2.011

3.1.4. Morphologic assessment of NiO_x layers through SEM analyses

To have a morphological assessment of the NiO_x , SEM analyses were performed on the four different NiO_x layers deposited over glass. The top view SEM images collected are shown in the Figure 7. In the top view SEM image of the NiO_x layers it is confirmed that the film appears to be quasi smooth, and uniform with closely packed spherical grains. However, there is evidence of a wrinkled pattern, which is due to the ITO film underneath the NiO_x layer since the thickness is so low. This is also evident in other works, using sputtered NiO_x[54].

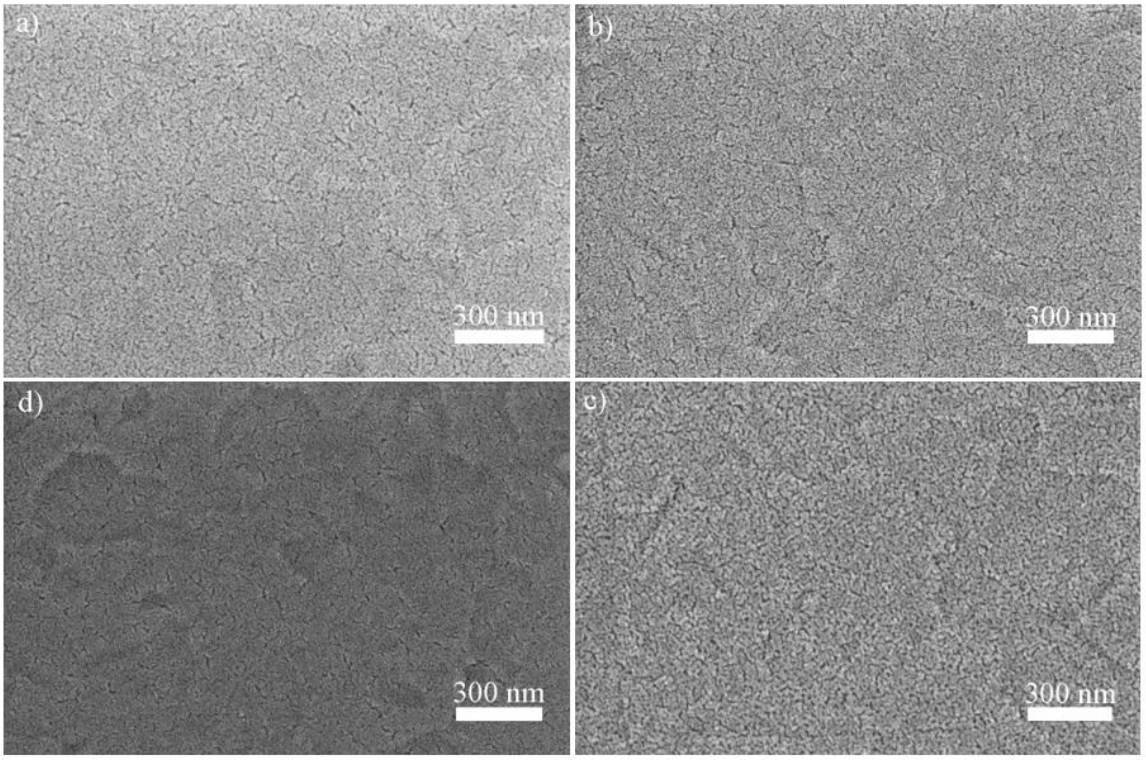

Figure 7 - SEM images on four NiO_x solutions deposited on a ITO substrate: a) Pristine NiO_x, b) Mg:NiO_x, c) Co:NiO_x, d)MgCo:NiO_x.

3.1.5. Crystal structure of NiO_x films

Moving on from the topographical characterization, the crystallinity of the four different NiO_x thin films was investigated. In order to do that an GIXRD analysis took place, using a 0.4º grazing angle.

Parallel to this, and complementing even more this study, the crystal sizes of each sample, were calculated by Scherrer's formula[57,58]. This formula dictates the grain size (diameter) of the crystals for each XRD peak, and it is as followed:

$$t = \frac{ks\lambda}{B\cos\theta} \quad (5)$$

$$2d\sin\theta = n\lambda \quad (6)$$

where t is diameter of the crystals (equation 5), present in the NiO_x thin films, λ is the X-ray wavelength (dependent on the equipment used - see Methods and Materials chapter 2.2.5), λ= 1.5406 Å, k_s is a shape factor constant in the range 0.8-1.2, since its typically equal to 0.9, we are going to consider this value, B is the peak width at FWHM and θ is the Bragg angle, that can be obtained by Bragg's law shown in equation (6).

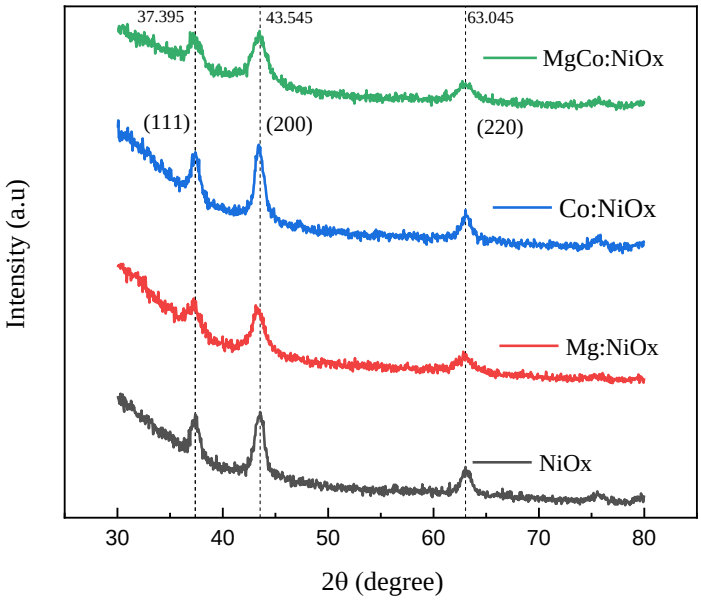

Figure 8 - XRD plots for the different NiO_x films deposit on glass

In Figure 8 there is a graphical representation of the X-ray diffraction peaks found when the 4 different NiO_x samples were analysed via GIXRD. These peaks, for all four samples, are located at 2Θ= 37.395º, 43.545º, 63.045º, 75.834º and 79.610º and represent, according to the literature[57,59],the (111), (200), (220), (311) and (221) crystalline planes of NiO_x respectively, proving the rock-salt cubic structure[44]. This perfect indexation of the crystal planes of cubic NiO_x phase indicates that the crystalline NiO was formed after heat treatment, like the annealing step that takes place right after deposition[57].

From analysing the GIXRD plots it is determined that in the pristine NiO_x, cobalt-doped NiO_x and co-doped samples the (200) plane represents the peak with the highest intensity, which means that the growth is dominated through this plane, that corresponds to the interplanar spacing d200= 0.2 nm[57]. However, for the magnesium - doped

NiO_x there is a slight shift in the preferential orientation of this film, from the (200) plane to (111) crystalline plane, such shift is also noticeable in other research that uses NiO_x doped with magnesium[44]. If we take a closer look at the intensity of the peaks, we can see that pristine NiO_x and cobalt-doped NiO_x exhibit the most intense peaks, indicating that those HTLs show a better crystalinity[60]. This supports the evidence shown in section 3.3 where undoped and cobalt based devices exhibited the best performance.

In Table 3, a summary of the calculated results from the information that XRD plot provides is displayed: The Braggs angle, given by 2Θ extracted directly from the plot, the FWHM for the three more intense peaks- (111), (200) and (220) in each sample, the calculated crystal size (diameter), using Scherrer's formula[57,58].

Table 3 - Resume table with: FWHM, crystal sizes and average crystal sizes for the 4 different films

HTL	***FWHM***			***Crystal size (nm)***		
	(111)	*(200)*	*(220)*	*(111)*	*(200)*	*(220)*
NiO_x	1.99	1.18	1.18	4.21	7.27	7.87
Mg:NiO_x	1.79	1.15	1.86	4.67	7.43	5.01
Co:NiO_x	0.89	0.98	0.74	9.44	8.76	12.66
MgCo:NiO_x	0.96	1.39	1.89	8.78	6.16	4.94

Comparing the values of the crystal size with the RMS values obtained via AFM, explored in the last subchapter 3.1.3, it can be noticed some correlation between the two characterization techniques. The same pattern observed in the RMS values, in which the Co:NiO_x presented the highest figure, Mg:NiO_x the lowest and seemed like when co - doping NiO_x with both magnesium and cobalt the effect that cobalt has is attenuated by the magnesium doping. This also happens with the average crystal sizes values. It was found that the sample with the largest crystals is Co:NiO_x and with the smallest is Mg:NiO_x. When combining the two doping agents, the effect of enlarging the crystals, provoked by cobalt, is as it appears, to be attenuated by magnesium. When comparing the obtained values with the ones in literature, Kaneko et al.[49] found that the average particle size in cobalt doped NiO_x is around 8 nm. For the same layer Marand et al. 2020[59] states that the values are between 11.5 nm and 12.4 nm, depending on the percentage of cobalt. Since the average value, for the cobalt doped NiO_x film, is 10.29 nm we can say that this value is not to far off from what it is stated in literature. Now comparing the magnesium based films with the data found in Li et al. 2017 [61], where a comparison between the crystal size of NiO_x and $NiMgO_x$ using the FWHM, in the (200) plane value, is outlined. Their conclusion is that values are in a range 10-14 nm, which does not align with these results. In Table 3 it is shown that the crystal size, in the (200) orientation, corresponds to 7.43 nm, which is not in the range of values given in literature. This is probably releated to the thickness of this layer, since magensium-doped NiO_x has wide peaks (high FWHM value) the measurement it is not very reliable. However In 2017, Li et al.[44] found that when doping NiO_x with 12% content of magnesium the XRD peaks (specially in (200) plane) seemed to have lost intensity and a similar effect happened were the peaks got wider.

3.2. Perovskite characterization

The absorbe layer was also a case study during this work in order to understand the coupling of the perovskite with the developed HTLs, and their behaviour in the final device. In this study, UV-Vis-NIR Spectrophotometry, XRD, Photo luminescence and SEM characterizations were undertaken.

3.2.1. Optical analysis

A UV-Vis-NIR Spectrophotometry analyses measurements were performed on $MAPbI_3$ layers deposited on ITO substrates, by transmittance and reflectance measurements. The data presented was used to determine the absorbance of each sample by using equation 7 bellow:

$$\text{Absorbance}(\%) = 100 - \{\text{Transmittance}(\%) + \text{Reflectance}(\%)\} \quad (7)$$

Plotting this provided the graph in Figure 9 a), which shows the absorbance data vs Photon Energy. Using the same thought process as before, the extrapolation of Tauc plot equation was also applied here. In which α represents the absorption coefficient, presented in equation (3). Since $MAPbI_3$ perovskites are direct bandgap semi conductor[62], n=1/2 in the Tauc equation described in equation (4), then we get:

$$(\alpha h\nu) = B(h\nu - Eg)^{\frac{1}{2}} \quad (8)$$

For the extrapolation above demonstrated, 245.6 nm was the value used for the thickness of the perovskite layer. This value was obtained during Mariana Moniz thesis using an image software on a SEM-FIB image, since the deposition settings and solutions used were the same, for the current study. The data was plotted, and we obtained the graph in Figure 9 b).

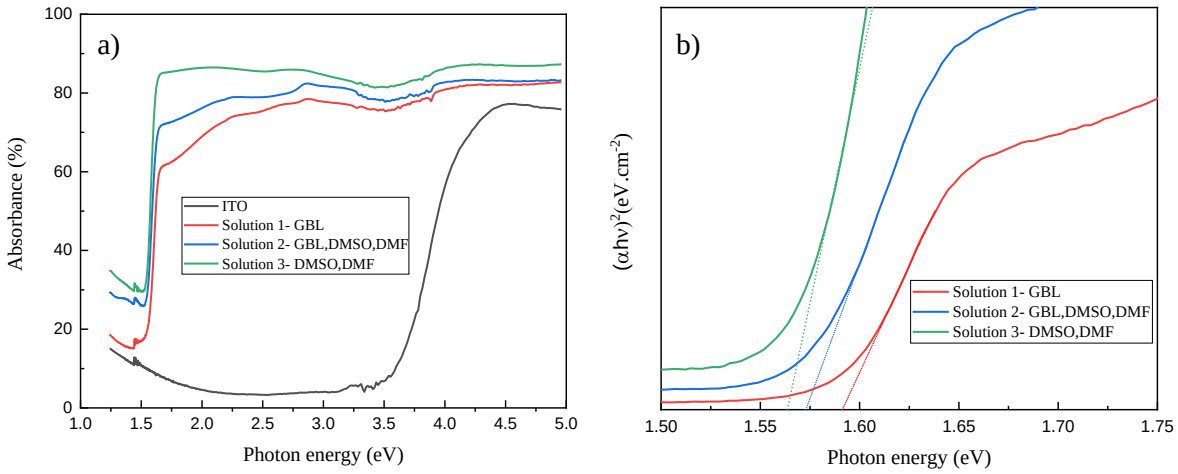

Figure 9 - a) Absorbance of the $MAPbI_3$ perovskite films, b) Tauc-plot for the $MAPbI_3$ perovskite films.

By plotting Tauc equation, the optical bandgap of three different $MAPbI_3$ perovskites layers were acquired. Using Origin Lab software, a linear fitting was performed on the high to low absorption transition region[63] of the obtained plot and intersected with the x-axis. This intersection gives us the optical bandgap of the perovskite films. In which for solution 1 is 1.59 eV, solution 2 is 1.57 eV and solution 3 is 1.56 eV. The obtained values are within

an acceptable range when comparing to the existing literature[64,65]. The transmittance, reflectance and absorbance vs wavelength plots of the perovskite thin films are available in the appendix section G of this document in Figure 27, Figure 28 and Figure 29, respectively.

After preparing samples of $MAPbI_3$ perovskites of solution 2 (described in the appendix section D) deposited on the four different types of NiO_x studied, photoluminescence spectroscopy was conducted. The PL spectra of perovskite films deposit on pristine and doped NiO_x layers and the bandgap values of each layers are displayed in Figure 10 and Table 4 respectively.

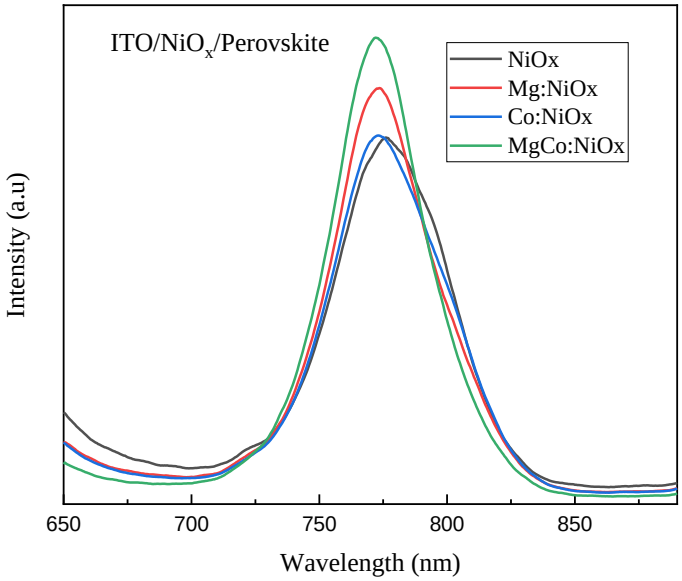

Figure 10 - Photoluminescent peaks of perovskite film over the four different NiO_x HTL's.

Table 4 - Resume table of the PL for $MAPbI_3$ perovskite films deposited on the four different HTLs

HTL	***Peak- Wavelength (nm)***	***Bandgap (eV)***
NiO_x	776	1.598
$Mg:NiO_x$	774.5	1.603
$Co:NiO_x$	773	1.604
$MgCo:NiO_x$	772	1.606

Dileep K et al.[65] considers PL a versatile tool to rapidly assess the photovoltaic activity of PSCs, so those findings were used to compare results. In this article it is considered a conventional peak at 770 nm which is attributed to the conventional characteristic emission of $MAPbI_3$. Since the data shows peaks in a range 772-776 nm it can be said, with some degree of confidence, that the calculated bandgap, is in agreement with literature[44,49,59,65,66]. One other information extracted from the plot in Figure 10, is that the more quenched peaks (lowest intensity) are the ones from pristine NiO_x and cobalt-doped film. This means that the perovskite layer over the undoped NiO_x and cobalt-doped layer has a more efficient charge transfer process which is related to a less radiative recombination of the charge carriers[67,68]. This is manifested in the performance figures (present in section 3.3 of this document) acquired by the devices with those HTLs, since were the ones with better performance .Some

researchers have also found evidence of this while working with cobalt doped NiO_x thin films in PCSs[46,48,59]. The bandgap results, here obtained, can also be comparable to the ones achieved via Tauc Plot. The data showed in Figure 9 b) yields a bandgap value of 1.57 eV, this value does not fall in the range of 1.598 eV-1.606 eV, presented in Table 4. It seems that the NiO_x layer, underneath the perovskite, slighly shifts the bandgap to higher.

3.2.2. Photoluminescence- Perovskite with and without PCBM layer as ETL

The same characterization was performed in two different set of samples. One set was prepared simply by depositing the perovskite film (solution 2 in appendix section D) over the four different NiO_x layers, and another set was prepared in the same way but with an additional PCBM layer (ETL) deposited over the perovskite.

Upon plotting the obtained data, a comparison between the charge extraction efficiency with and without the PCBM ETL, over the structures with different HTLs can be withdraw. The graph in Figure 11 shows the steady-state PL spectra of perovskite and perovskite/PCBM samples.

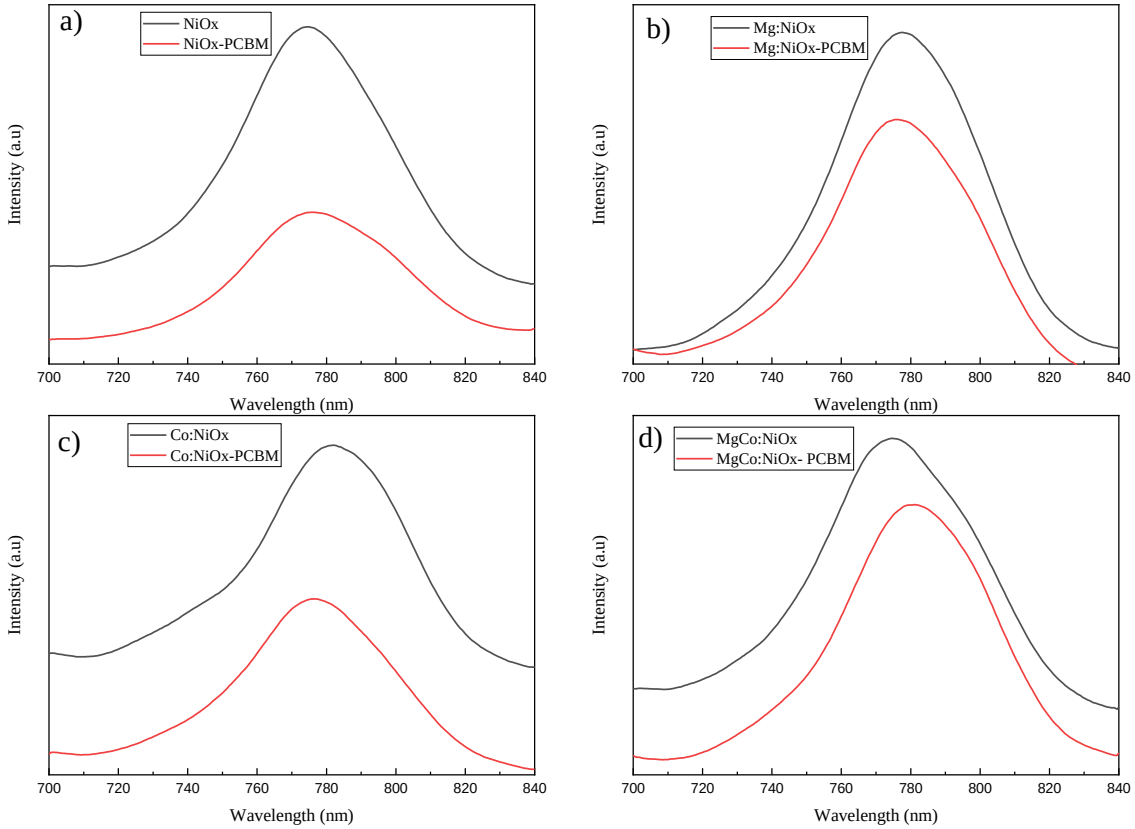

Figure 11 - Steady-state photoluminescence (PL) of perovskite and perovskite/PCBM on top of a)Pristine NiO_x, b) Mg:NiO_x, c) Co:NiO_x and d) MgCo:NiO_x.

These plots show that when the PCBM layer is formed over the perovskite layer, a quenching effect happens, which indicates an efficient charge transfer process at the perovskite/PCBM interface. This is facilitated by less radiative recombination of photo-generated electrons[67,68]. By analysing the difference in the intensities of each plot, this effect is more evident in the undoped NiO_x and Co: NiO_x. The devices fabricated with those layers (explored in section 3.3) were responsible for achieving the best performance results. The Mg:NiO_x and co-doped sample shows a minimal quenching effect. In 2017 Liu et al.[69]also observed and studied this effect, this time using PEDOT:PSS as an HTL instead of NiO_x. In Table 5, there is a resume of the peaks, and correspondent wavelength

obtained from the PL plot. From the information present in Table 5 there is a small shift, almost minimal. When this deviation goes from a higher wavelength to a lower one, it is expected an improvement in the film morphology, with a reduction in surface trap states on the interfaces of perovskite layer[68].

Table 5 - Resume table of the peaks represented in the graph of Figure 14

	Peaks (nm)	
HTL layer	*Perovskite*	*Perovskite/PCBM*
NiOx	774,5	776
Mg:NiOx	777,5	776
Co:NiOx	782	776,5
MgCo:NiOx	781	774.5

3.2.3. X-ray Diffraction- of Perovskite layer

The crystallinity of the perovskite layer was also analysed by preparing samples of $MAPbI_3$ perovskite (Solution 2 in the appendix D) deposited on the four different NiO_x over ITO substrates. The XRD pattern, with the respective peaks, of our $MAPbI_3$ perovskite layers are represented in Figure 12.

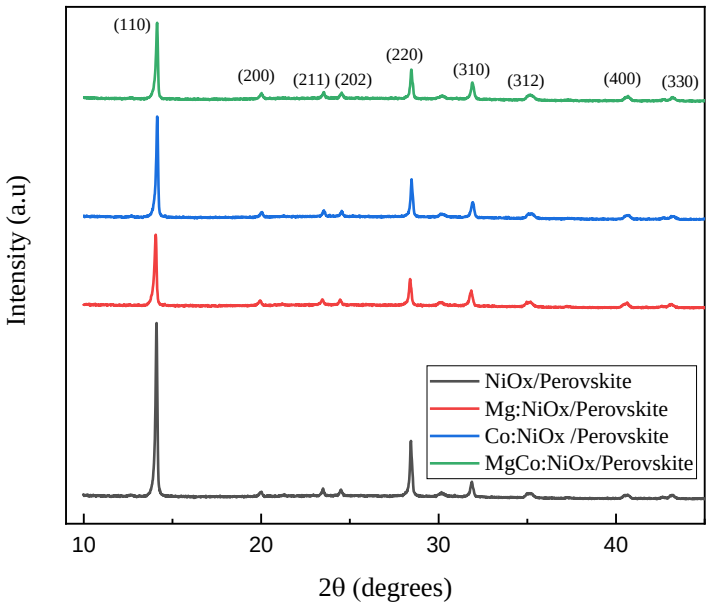

Figure 12 - XRD pattern of Perovskite layer deposit on top of four different NiO_x films.

The plot, above represented in Figure 12, shows the XRD pattern of the perovskite layer over the four different HTLs, with the respective peaks represented. The data shows peaks located at 14.16º, 20º, 23.48º, 24.52º, 28.44º, 31.87º, 35.15º, 40.62º and 43.20º corresponding to (110), (200), (211), (202), (220), (310), (312), (400) and (330) respectively, that are compatible with the current literature[65,70–73].

The typical peaks, corresponding to the planes (110), (211), (220), are due to the tetragonal phase of the perovskite[70]. The preferential growth planes are (110) and (220) since those are the highest intensity peaks[70].It is also noticible that, as shown in the NiO_x GIXRD plot, that both pristine NiO_x and cobalt-doped NiO_x exhibit the most intense peaks. This benefits the growth of the perovskite crystal allowing for larger grain sizes and good orientation, something explored in more depth in SEM characterization in section - SEM analysis of Perovskite layers 3.2.4. It is also relevant to prove why both cobalt-doped and pristine NiO_x based devices showed the highest PCE values.

To confirm these peaks, and to make sure they are not misrepresented, the same perovskite solution was spin coated on top of a glass substrate in order to performe XRD on it and shown in Figure 13.

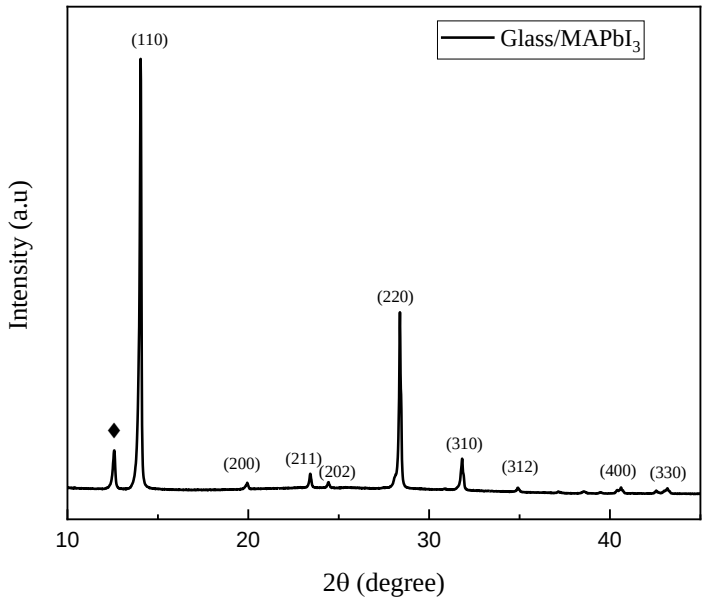

Figure 13 - XRD pattern of perovskite layer deposit on top of a glass substrate

After analysing the plot in Figure 13 the peaks corresponding to the angles of: 14.05º, 19.94º, 23.42º, 24.41º,28.38º, 31.83º 34.90º, 40,62º and 43.19º corresponding to (110), (200), (211),(202), (220), (310), (312), (400) and (330), respective, are represented. Many researchers found the same information[65,70,71,73] and in Guo et al. 2016[73] it is found very detailed information regarding the XRD peaks of the $MAPbI_3$ film. Upon examining Menda et al. work[74] it is confirmed that the peak situated at 12.59º, represented by a black diamond in Figure 13, is in fact due to a photoinactive PbI_2. This analysis provided confirmation of the previous XRD measurements performed on perovskite over NiO_x thin films.

3.2.4. SEM analysis of Perovskite layers

In order to visualize and calculate the size of the grains present in the perovskite layer, SEM analysis of this layer ($MAPbI_3$- solution 2 of apendix section D) was conducted. Using Image J software on the images present in Figure 14, the length of 30 crystal grains were measured, and the respective average grain size for each film was determined. The perovskite deposit over the pristine layer of NiO_x was found to have higher average size at 382.25 nm compared to the 254.85 nm of the layer deposit on the co - doped HTL of MgCo:NiO_x. This is associated to the

XRD patthern, shown in the previsous subchapter, that determined perovskite films grown on top of undoped NiO_x delivered the highest intensity peaks, which leads to the formation of bigger perovskite grains with reduce grain boundaries[59]. Given that there is a lot of morphological irregularity between grain sizes an histogram to show size distribution is also available.

In the current literature there is evidence that the NiO_x layer doped with cobalt enlarges the perovskite grains. Marand et al. 2020[59] and Choi et al. 2021[27] verified that with an increase of doping percentage in the NiO_x and doping this layer, respectively, the perovskite grains seemed to get bigger[27,48,59]. This doesn't seem to happen in this case given that the average perovskite grain size is higher in the layer over an undoped NiO_x HTL.

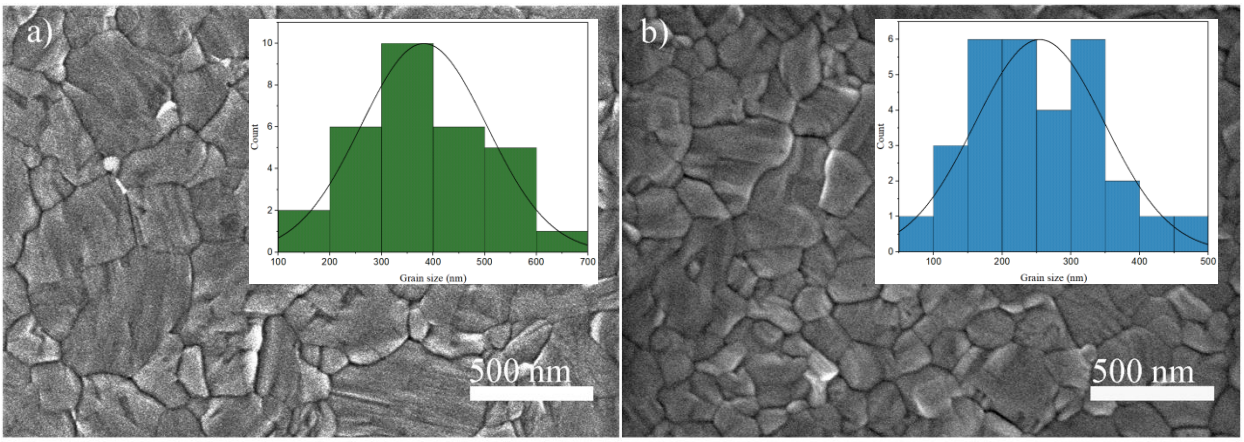

Figure 14 - Top view SEM images of $MAPbI_3$ perovskite layer deposited over: a) pristine NiO_x and b) co-doped NiO_x. The inset histograms show the grain size distribuition for each sample.

3.3. Perovskite Solar Cells- Fabrication and charactherization

The fabrication of devices took place using the same NiO_x deposition parameters, evident in the Methods and Materials section, to deposit the characterized films, mentioned before.

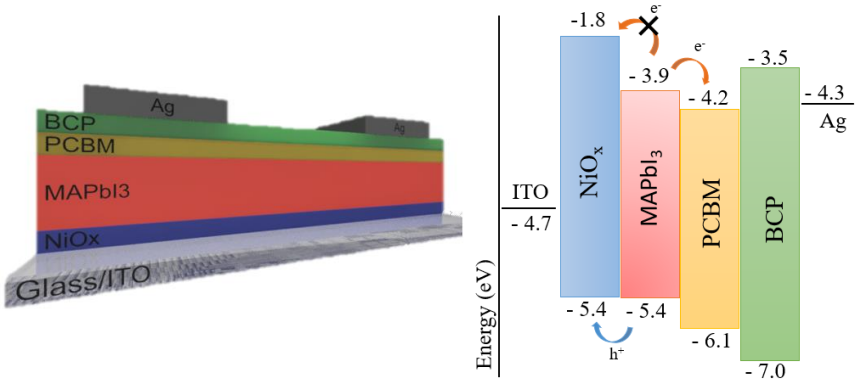

Figure 15 - Schematic of the fabricated solar cell and correspondent energy band diagram[75,76].

The fabrication of a PSC must take into consideration many factors, two of them being: the use of high temperatures and its architecture/structure. In this thesis, due to the requirement of an annealing step for the NiO_x film that occurs at 450 ºC for 1 hour, only rigid substrates such as ITO and FTO coated glasses were used as substrates. After analysing the work presented by Guo et al. in 2018[77], and some investigation, the use of ITO seemed to be a better proposition. It appears that ITO prevents the increase of the sheet resistance during the high-temperature treatment of NiO_x film, such as the annealing step at 450ºC, which leads to high FF ultimately improving PCE value[77]. The AFM data, which is shown in the appendix section F, showed that FTO has a higher RMS than ITO, and that this also extends to the NiO_x thin films deposit on each one of these substrates. As demonstrated in literature[15,34], the higher RMS value of the FTO is correlated to an increase in roughness of this layer, which also makes the roughness of the NiO_x film[41,78] to increase.

Those substrates are also ideal for an inverted superstate configuration like the one fabricated, since this is the first layer that meets the light, it needs to be optically transparent to optimize photocarrier generation in the perovskite layer[15].

As mentioned before the focus of this work was on inverted perovskite solar cell devices, this means that the first solution being spin coated on the *Glass/ITO* substrate is the HTL, like it is demonstrated in the schematic of Figure 15. After the HTL, a precursor solution of $MAPbI_3$, PCBM (ETL) and BCP (buffer layer) are respectively spin coated onto the NiO_x thin film. 100 nm of silver top contact was deposited by thermal evaporation in high vacuum ($< 6x10^{-6}$ mbar) to finalize the fabrication of the devices. The BCP buffer layer is proven to be useful, using a critical thickness of 5 nm, since it enhances the performance of planar inverted PSCs, due to the formation of an ohmic contact and reduction of interfacial charge recombination effect of BCP buffer layer[76].

To facilitate the spread of the NiO_x and perovskite solutions a UV-Ozone treatment over the ITO substrate was applied, prior to the NiO_x deposition. This strategy was already thoroughly investigated by other researchers[33,34,41–43], for example, in 2019, Wang et al.[41]demonstrated that this UV-Ozone surface treatment, increases the surface wettability, electrical conductivity, and work function of the prepared NiO_x film. When applied to the NiO_x layer, benefits for good coverage of perovskite layer, leading to efficient extraction of photogenerated holes from the light absorber layer and low interfacial recombination. Taken this into consideration this strategy was applied prior to the deposition of NiO_x (on ITO substrate) and before the perovskite deposition (on NiO_x).

3.3.1. Influence of HTL annealing equipment on PSC performance

In parallel to the characterization of the NiO_x layer with UV-Vis-NIR spectrometry a batch of devices was fabricated using three different equipments to anneal the four HTL layers: furnace (Nabertherm), hot plate and tube furnace. The following devices were characterized under a solar simulator to obtain the JV curves, and their respective performance figures: V_{OC}, J_{SC}, FF, and PCE. In Figure 16 we show the graphs for each NiO_x sample annealed using three annealing equipments.

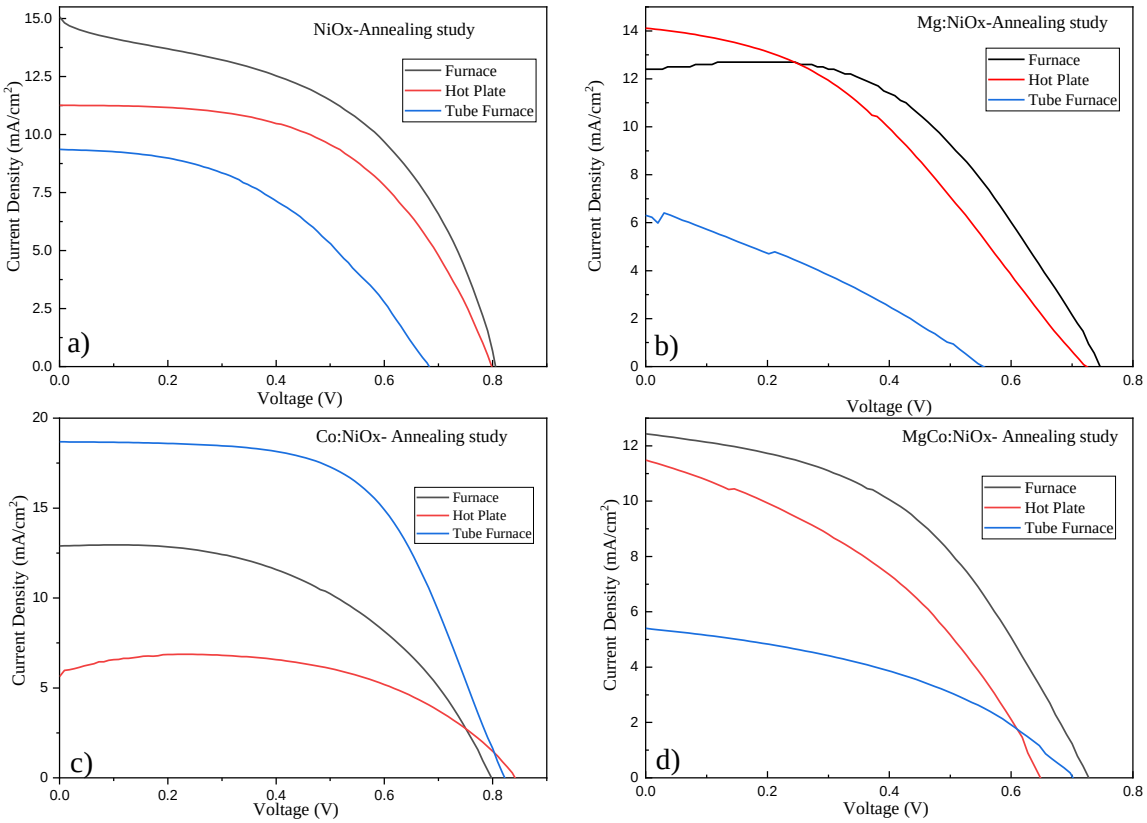

Figure 16 - JV curves showing devices with the different doping and the different annealing equipment. a) pristine NiO_x, b)Mg:NiO_x, c) Co:NiO_x, d) MgCo:NiO_x.

Table 6 - Values extrapolated from the JV characterization (using equations in appendices A) of best-performing PSC, in annealing study, with NiOx, Mg: NiOx,Co: NiOx and MgCo: NiOx.

	NiO_x				$Co:NiO_x$			
Equipment	***V_{oc}***	***J_{SC}***	***FF***	***PCE (%)***	***V_{oc}***	***J_{SC}***	***FF***	***PCE(%)***
Furnace	0.80	14.82	0.49	5.89	0.80	12.96	0.50	5.14
Hot Plate	0.80	11.28	0.54	4.86	0.84	5.84	0.64	3.14
Tube	0.68	9.40	0.45	2.88	0.83	18.70	0.59	9.06
	$Mg:NiO_x$				***$MgCo:NiO_x$***			
Equipment	***V_{oc}***	***J_{SC}***	***FF***	***PCE (%)***	***V_{oc}***	***J_{SC}***	***FF***	***PCE (%)***
Furnace	0.73	12.46	0.46	4.17	0.75	12.42	0.51	4.73
Hot Plate	0.73	14.16	0.38	3.97	0.79	11.20	0.52	4.57
Tube	0.70	5.41	0.42	1.58	0.55	6.31	0.33	1.15

To resume the data obtained from the graphs above illustrated, Table 6 represents the performance values for the best device with: pristine NiO_x, Mg:NiO_x, Co:NiO_x and MgCo:NiO_x for each equipment respectively.

From the information present on Table 6, the device with cobalt-doped NiO_x had the highest efficiency at 9.06%. Although this might be a coincidence since in other batches, the pristine NiO_x was the best device out of the four. In the statistical study section, the data related to this batch is also present, a closer look at that data can confirm that the undoped NiO_x exhibited the higher average PCE values. To help this thesis, a quick EDS scan (not available in this thesis) was perfomed and it was found a minimal percentage of cobalt in the doped thin film. This seems to indicate that the doping was not present enough to show effectiveness.

There is also a noticeable problem when using the tube furnace and hot plate with many substrates at once. The heat distribution throughout the samples is not equal, which means that some substrates might be at a higher temperature than others. The only way to mitigate this problem is by annealing less samples at once, which does not happen in the furnace (Nabertherm) since it is a closed system with a larger area, allowing for up to 24 substrates to be annealed at the same time.

3.3.2. Light soaking effect on PSCs

When assessing the performance of a device many researchers agree that light soaking (LS) is an effect worth exploring[34,79,80]. Wenger et al.[80] even considers this an important tool to assess a solar cell performance. Knowing this, the effect that light soaking has on the device performance was investigated. Using the data gathered from 4 different batches (with 13 to 15 devices analysed per NiO_x HTL) the best devices J-V curves were plotted and are present in Figure 17 with light soaking prior to the measurements and without it.

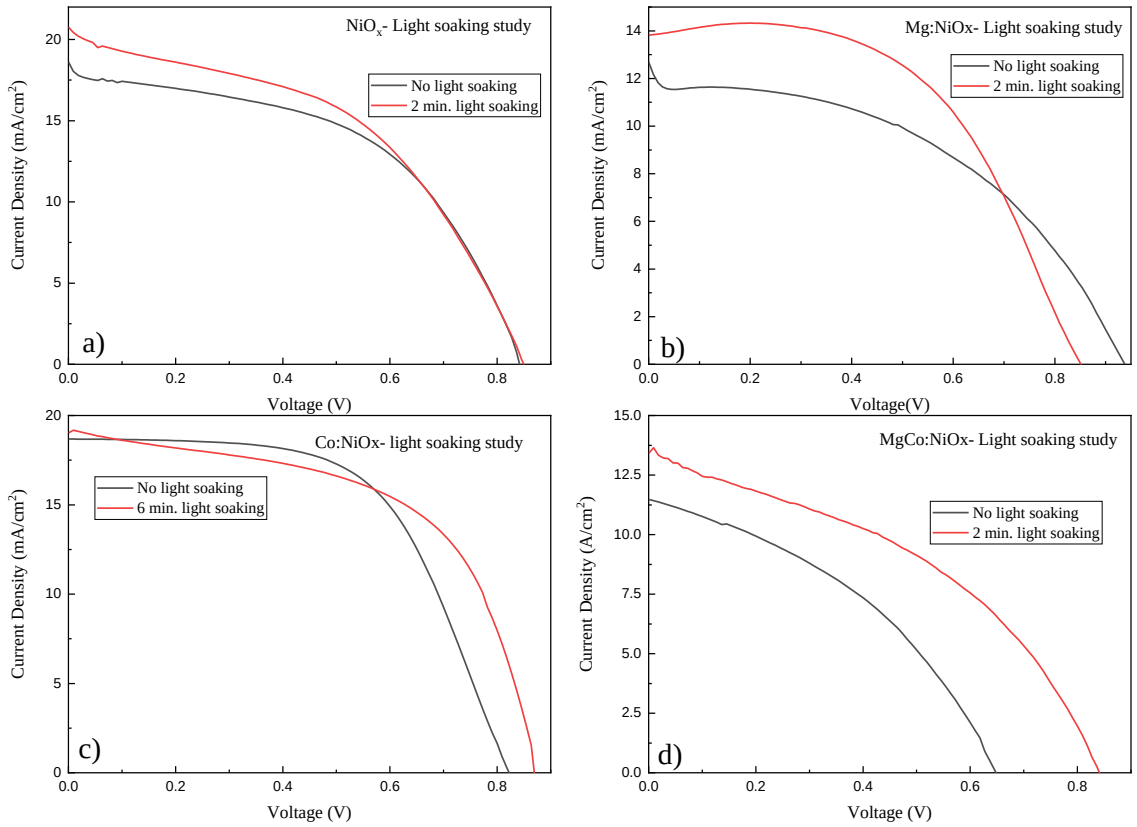

Figure 17 - J-V curves comparison of the best devices using light soaking and not using it, for : a) NiO_x, b) Mg: NiO_x, c) Co: NiO_x and MgCo: NiO_x.

Table 7 - Resume table with the performance figures of the best devices with and without light soaking.

	V_{oc} (V)		**J_{SC} (mA/cm²)**		**FF**		**PCE (%)**	
HTL	*No LS*	*LS*	*No LS*	*LS*	*No LS*	*LS*	*No LS*	*LS*
NiO_x	0.84	0.85	17.96	20.40	0.51	0.47	7.78	8.14
Mg: NiO_x	0.94	0.85	11.79	13.89	0.47	0.54	5.22	6.45
Co: NiO_x	0.83	0.87	18.70	19.11	0.59	0.57	9.06	9.49
MgCo: NiO_x	0.65	0.84	11.49	13.52	0.40	0.41	2.94	4.61

From the data present in Table 7 it is observed that light soaking the devices prior to the measurement can enhance some of the performance figures of the devices. This is already studied by Tsai et al.[79], where it was found that continuous light illumination leads to a uniform lattice expansion in hybrid perovskite thin films that culminates in enhancing the performance figures in PSCs devices. In Zhao et al. 2015 article[81] it is stated that the light soaking and hysteresis effects come from charge trapping rather than the increase in temperature that the device encounters when exposed to light. It is also evident in this work that the V_{OC} is a figure that tends to increase with light exposure. This happens due to a result of decrease in photogenerated charge carriers at the electrodes interfaces. It is suggested that those carriers can neutralize the interfacial defects and consequently increase V_{OC}[81]. In the conducted experiments, this did not happen exactly like both researchers[79,81] portrayed. When light soaking is provided to the devices, prior to the measurements, PCE and J_{SC} values increase in all of them, giving us the record PCE value of 9.49% in a device using cobalt-doped NiO_x and 20.40 mA/cm² of J_{SC} in a device using a pristine NiO_x

layer. A closer look at the V_{OC} values, in Table 7 also shows an improvement, except for the magnesium-doped NiO_x HTL device. However, the statistical studies, presented by the box charts in Figure 18 and Figure 19 show a different scenario, this figure only increases, on average, on cobalt-doped and co-doped NiO_x devices. The FF value in these specific devices increases in the magnesium-doped and co-doped NiO_x devices and decreases in the rest of the devices, which is something that contradicts the current literature[79,81,82]. During the experiments it was found that PSCs have a time threshold for the light soaking. If we expose the devices for a certain period of time the performance of those cells will be affected, this was investigated by Deng et al.[82] in 2018. It was found that the concentration of pre-accumulated ions can be minimized by light soaking because an annihilation of this ions occurs rapidly within tens of seconds. This process improves both J_{SC} and V_{OC}. However, after prolonged light exposure, negative ions drift to the HTL/perovskite interface causing a decrease in performance. This is caused by the increased trapping by defects at the interface due to either increased ionic traps or capture of carriers at the interface[82].

Using the data available, the box charts present in Figure 18 and Figure 19 with no light soaking and with light soaking prior to the measurements, respectively, were obtained. This allows for a statistical study to be conducted, that evaluates the distribution of values for each type of device and to see if the results can be reproducible.

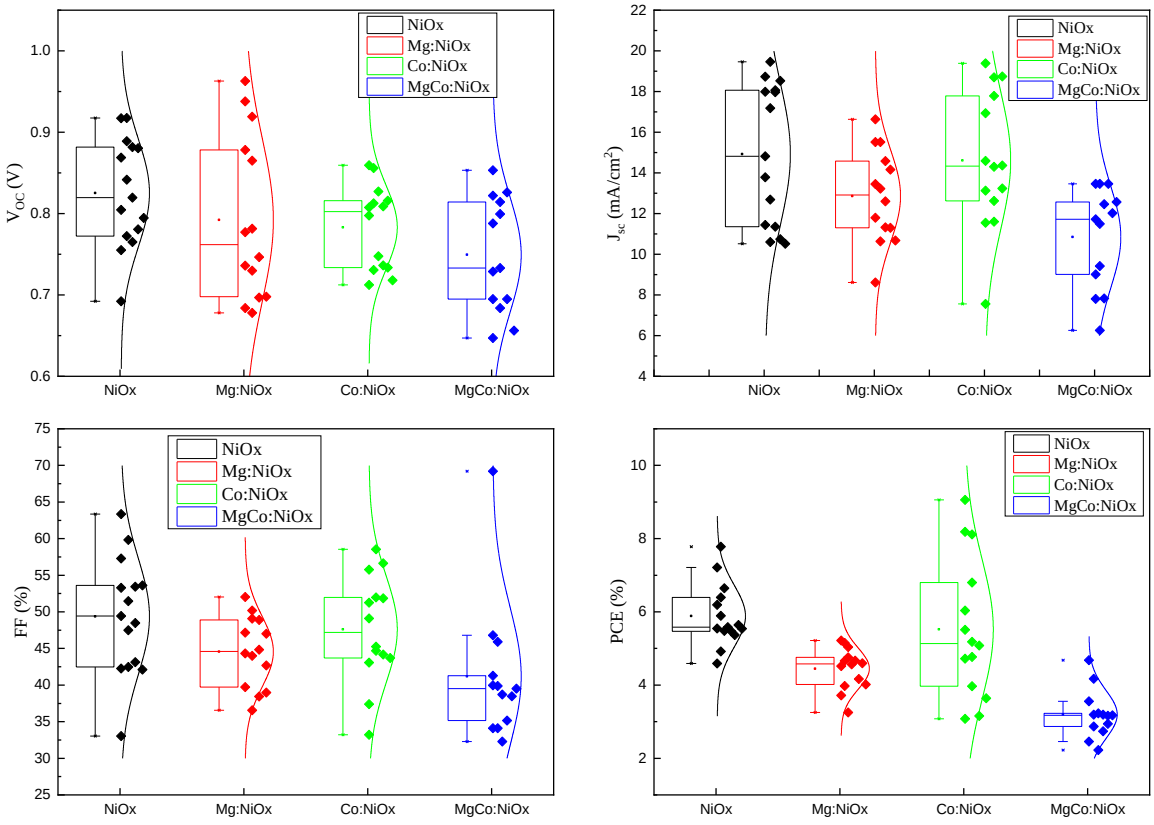

Figure 18 - Box chart of the distribution of the PCE, V_{OC}, J_{SC}, and FF values of devices using four different HTL's: NiO_x, Mg: NiO_x, Co: NiO_x and MgCo: NiO_x.

Using the data available, the box charts present in Figure 18 and Figure 19 with no light soaking and with light soaking prior to the measurements, respectively, were obtained. This allows for a statistical study to be

conducted, that evaluates the distribuition of values for each type of device and to see if the results can be reproducible.

From looking at Table 7 and Figure 18 it can be seen that, the PCE value the undoped NiO_x showed the higher average value at 5.88% and the co doped devices the lowest at 3.20 %. Although the cobalt-doped devices represented the record PCE value, in a single solar cell, that was not represented in the average number. It is also noticeable that it has the highest variability ranging from 3.08% to 9.06%. However, since the variation between the 75% percentile and 25% percentile (top and bottom values of the boxes) is smaller we can conclude that the depositions seemed to be more uniform in this case.

The V_{OC} plot, shows the magnesium-doped NiO_x device to have the record value and highest variability at 0.96 V and 0.68 – 0.96 V respectively. However, once again, the pristine NiO_x devices record the highest average value of 0.83 V. The same thing happened regarding the FF percentage, where this device scored the highest average value of 0.49 ranging from 0.33 to 0.63. From J_{SC} data, the highest variability is achieved by the cobalt devices with values from 7.56 mA/cm^2 to 19.39 mA/cm^2. The average value on these devices was of 14.61 mA/cm^2, which is close to the highest average value, achieved once again, by the undoped NiO_x devices with 14.92 mA/cm^2.

Since light soaking has been one of our focuses in this work, the same analysis as before, for the same devices, was made, this time with light soaking the devices prior to the measurements. In Figure 19, we present the box chart for this study.

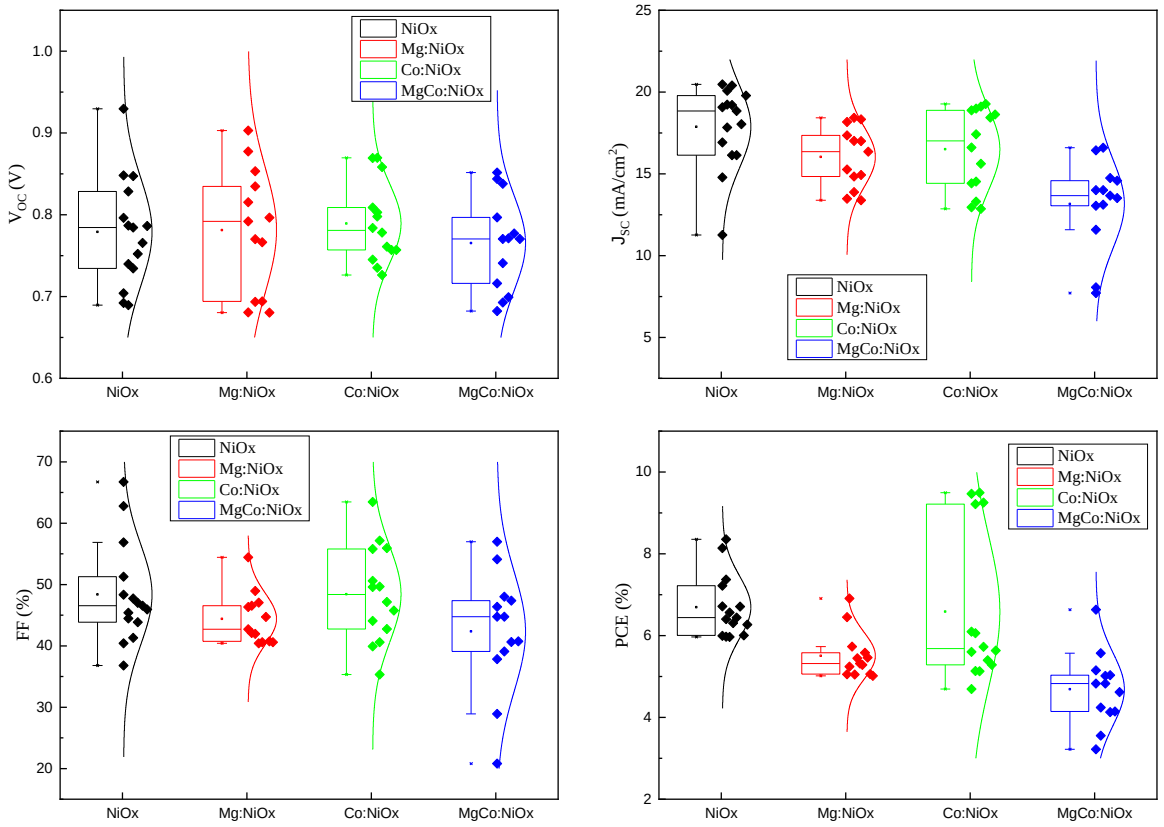

Figure 19 - Box chart of the distribution of the PCE, V_{OC}, J_{SC}, and FF values of devices using four different HTL's: NiO_x, Mg: NiO_x, Co: NiO_x and MgCo: NiO_x, using light soaking prior to the measurements.

By comparing Figure 18 and Figure 19, it is clear the impact that light soaking has on the solar cells performance. Comparing the two box charts and the values compiled in Table 7 it can be assessed that light soaking enhances, primarily, the current density and PCE. Many researchers[79,81,82] show that J_{SC}, PCE also increased over light soaking exposure. A reflection of this is proven with the increase of the average values for each type of devices. However, their data seems to disagree with our results: For the V_{OC} values, in our case, light soaking does not always cause an increase. With light soaking, these figure increases in the cobalt-doped and co-doped devices by 0.01V and 0.02V, respectively. This seems to slightly contradict the data compiled in Table 7, which shows the importance of conducting statistical studies. Comparing the percentile boxes in Figure 18 and Figure 19 there is a shift in the PCE variation between the 75% percentile and 25% percentile, in all samples. In the case of cobalt-doped devices this variation is noticeable, in which the two percentiles become uneven. Usually this is an indication of lack of uniformity in the deposition, but since the devices used were the same, this outcome indicates a nonuniformity in the actual conduct of the light soaking test. To mitigate this problem, an automated procedure should take place, where the minutes of exposure could be precisely controlled and remained unchanged for all measurements. For the other type of devices light soaking seems to improve the ratio between the two percentiles. Regarding the performance figures, the increasing tendency, verified in Table 7, is also confirmed here by the increase of average PCE values. Where it goes from 5.88% to 6.69% , 4.45% to 5.51%, 5.52% to 6.59% and 3.20% to 4.69% as a percentage of PCE of the NiO_x, Mg: NiO_x, Co: NiO_x and MgCo: NiO_x devices respectively, without lightsoaking and with light soaking.

4. Conclusions and future perspectives

This project aimed to develop an high efficiency, stable and low-cost inverted *p-i-n* planar PSC. The efforts were focused on optimizing and comparing 4 different NiO_x HTLs. In order to do that, doped and co-doped layers with magnesium and cobalt were developed.

To fabricate such devices, spin coating was used to deposit all layers, apart from the ITO and silver top contact in the solar cells structure given as – *ITO /HTL/Perovskite/PCBM/BCP/Ag*. The parameters used were also searched in the literature, and some of them modified to serve this thesis needs, which are explicit in the Methods and Materials section of this report. To optimize the different NiO_x materials, several characterization techniques were employed. From the optical analysis of the HTLs, it was assessed that the doping caused the bandgaps to slightly increase by 0.06 eV, 0.04 eV and 0.03 eV for cobalt-doped NiO_x, magensium-doped NiO_x and co-doped HTL respectively. The evidence gathered from the GIXRD analysis performed on the four types of NiO_x indicated that the pristine NiO_x and cobalt-doped NiO_x presented a better cristalinity. The same is evident for the subsequently-deposited perovskite material, since the samples with more intense peaks were the ones deposited over undoped NiO_x and cobalt- doped NiO_x, which implies better perovskite crystalinity resulting in larger grain sizes. Which was confirmed in the SEM images (section 3.2.4) of the perovskite laid over an undoped NiO_x layer. The PL characterization on perovskite layers over NiO_x also indicated that the best results were on cobalt-doped NiO_x and pristine NiO_x. These samples exhibited a pronounced quenching effect, which indicates a more efficient charge carriors extraction process. The same effect was more evident, on the same type of samples (using pristine NiO_x and cobalt-doped NiO_x), this time after the PCBM deposition over the perovskite layer.

Since the focus of this thesis was towards the HTL, devices were fabricated using three different annealing equipments in the HTL manufacture: furnace (Nabertherm), hot plate and tube furnace. The use of a tube furnace to anneal the NiO_x films provided the performance record device, using a cobalt - doped NiO_x HTL – reaching a PCE of 9.06%. However, the Nabertherm furnace proved to be a better option, because it allowed annealing several samples at the same time, while maintaining good performance figures on average.

A statistical study, that takes into account all light soaked devices manufactured, revealed that the overall best devices (on average) were the ones employing pristine NiO_x, reaching an average PCE, J_{SC}, V_{OC} and FF values of 6.69%, 18.88 mA/cm^2, 0.78 V and 0.48.

Considering that solar cells are often exposed to sun light for long periods of time, light soaking phenomenon was studied by exposing devices to light prior to the measurements. The average data, implies that J_{sc} and PCE (%) increased in all devices, while V_{OC} and FF only improved in the Co:NiO_x and MgCo:NiO_x based devices. This experiment provided the best PCE result, from a device using cobalt-doped NiO_x as an HTL. The value increased from 9.06% to 9.49% after 6 minutes of exposure to the light prior to the measurement. The best J_{SC} result, at 20.41 mA/cm^2, occurred using light soaking on a device with pristine NiO_x layer. For V_{OC}, a maximum of 0.96 V was achieved with a magnesium-doped NiO_x based device. While a maximum of 0.69 regarding FF was obtained by a co-doped NiO_x solar cell.

4.1. Future Perspectives

In view of further complementing this study, and since we are exploring doping mechanisms, it would be interesting to conduct more characterizations on the HTL, in order to have a better understanding of the band structure and work function of the NiO_x layers. To achieve this, Ultraviolet Photoelectron spectroscopy (UPS), along with UV–Vis absorption spectrometry, should provide enough data to investigate how the surface electronic structures and work functions behave. This would lead to a full understanding on how the energy diagrams of functional NiO_x layers change according to the type and percentage of doping[40,49]. An additional important measurement that should have been conducted is X-Ray photoelectron spectroscopy (XPS), since ionic composition is an important information to have when doping a compound[26,27,34,46,49]. This technique provides the analysis of the ionic composition of NiO_x, and its dopants, with that the effects on its *p*-type nature can be measured. When performing XPS on a NiO_x film 3 peaks are expected: a peak at 860.8 eV corresponds to the shakeup process in the NiO_x structure; at 853.6 eV is ascribed to the Ni^{2+} ions in the standard Ni─O octahedral bonding configuration; at 855.5 eV, attributed to the Ni^{3+} ions and due to the presence of Ni^{2+} vacancies this could be fitted with two peaks at 856.3 and 855.0 eV, corresponding to NiOOH and Ni_2O_3, respectively[26]. Regarding cobalt doping, Kaneko et al. 2019[49] analysed the XPS spectra of Co-NiO_x nanoparticles. found Co $2p_{1/2}$ and $Co2p_{3/2}$ peaks at around 795 and 780 eV, respectively[27,49]. If the same characterization tool is used on magnesium-doped NiO_x thin films, a Mg 1 s peak at 1301.4 eV is expected to be detected[27]. The XPS spectrum of O 1s core level usually consists of two peaks centered at 529.2 eV, for Ni-O octahedral bonding and 531.0 e,V for Ni^{3+} which is also decomposed in two peaks centered at 531.1 eV and 530.8 eV, corresponding to the O 1s in NiOOH and Ni_2O_3, respectively[26]. Unfortunately there was no time to conduct such characterizations in the time frame available, and devices manufacturing and other characterizations were prioritized.

One unfortunate impossibility of this work was to properly acquire the thickness for every layer in the fabricated device. This was not possible because the equipments need it (SEM-FIB and perfilometer) were unavilable at the time. To have proper information regarding this it is adviced to perform perfilometer measurements on the HTLs and also SEM-FIB cross section images on the complete device in order to guarantee a visual confirmation of the thickness of each layer.

A missing target of this work was to dope the NiO_x layer in a significant matter. We believe that the major problem lies in the incorporation of cobalt, since a quick EDS measurement, showed a low percentage of this compound in the thin film. Many researchers tend to incorporate different percentages, and higher ones, compared to the ones used in this work, of cobalt[48,49] in their NiO_x precursor solutions, this might represent a more adequate strategy. For magnesium, the opposite should be done. Li et al. 2017[44] states that magnesium content over 12% is detrimental to the crystallinity of the film, so to stay below this threshold, less content of magnesium should be added to the precursor solution.

To take this work further in terms of its applicability, low temperature and solution-processable methods should be consider allowing the use of flexible substrates such as PET and other polymer solutions[33,34,83,84].

References

1. Schwab, K. *The Global Competitiveness Report*. *World Economic Forum* (2018).
2. Ansari, M. I. H., Qurashi, A. & Nazeeruddin, M. K. Frontiers, opportunities, and challenges in perovskite solar cells: A critical review. *Journal of Photochemistry and Photobiology C: Photochemistry Reviews* **35**, 1–24 (2018).
3. Yin, X., Guo, Y., Xie, H., Que, W. & Kong, L. B. Nickel Oxide as Efficient Hole Transport Materials for Perovskite Solar Cells. *Solar RRL* **3**, 1–27 (2019).
4. Saliba, M. *et al.* How to Make over 20% Efficient Perovskite Solar Cells in Regular (n-i-p) and Inverted (p-i-n) Architectures. *Chemistry of Materials* **30**, 4193–4201 (2018).
5. best-research-cell-efficiencies.20190802.pdf.
6. Katz, E. A. Perovskite: Name Puzzle and German-Russian Odyssey of Discovery. *Helvetica Chimica Acta* **103**, (2020).
7. Gao, P., Grätzel, M. & Nazeeruddin, M. K. Organohalide lead perovskites for photovoltaic applications. *Energy and Environmental Science* **7**, 2448–2463 (2014).
8. Gharibzadeh, S. *et al.* 2D/3D Heterostructure for Semitransparent Perovskite Solar Cells with Engineered Bandgap Enables Efficiencies Exceeding 25% in Four-Terminal Tandems with Silicon and CIGS. *Advanced Functional Materials* **30**, (2020).
9. Kim, H. S. *et al.* Lead iodide perovskite sensitized all-solid-state submicron thin film mesoscopic solar cell with efficiency exceeding 9%. *Scientific Reports* **2**, 1–7 (2012).
10. Kazim, S., Nazeeruddin, M. K., Grätzel, M. & Ahmad, S. Perovskite as light harvester: A game changer in photovoltaics. *Angewandte Chemie - International Edition* **53**, 2812–2824 (2014).
11. Song, Z., Watthage, S. C., Phillips, A. B. & Heben, M. J. Pathways toward high-performance perovskite solar cells: review of recent advances in organo-metal halide perovskites for photovoltaic applications. *Journal of Photonics for Energy* **6**, 022001 (2016).
12. Xing, G. *et al.* Long-range balanced electron-and hole-transport lengths in organic-inorganic CH3NH3PbI3. *Science* **342**, 344–347 (2013).
13. Ru, P. *et al.* High Electron Affinity Enables Fast Hole Extraction for Efficient Flexible Inverted Perovskite Solar Cells. *Advanced Energy Materials* **10**, 1–9 (2020).
14. Li, M. H., Shen, P. S., Wang, K. C., Guo, T. F. & Chen, P. Inorganic p-type contact materials for perovskite-based solar cells. *Journal of Materials Chemistry A* **3**, 9011–9019 (2015).
15. Fu, F. *et al.* High-e ciency inverted semi-transparent planar perovskite solar cells in substrate configuration. **1**, (2016).

16. Huang, L. *et al.* Solar Energy Materials & Solar Cells Ef fi cient electron-transport layer-free planar perovskite solar cells via recycling the FTO / glass substrates from degraded devices. *Solar Energy Materials and Solar Cells* **152**, 118–124 (2016).

17. DOI: 10.1002/ ((please add manuscript number)) Article type: Full Paper Development of a Perovskite Solar Cell Architecture for Opaque Substrates. doi:10.1002/solr.202000385.

18. Chiril, A. *et al.* Highly efficient Cu (In , Ga) Se 2 solar cells grown on flexible polymer films. *Nature Materials* **10**, 857–861 (2011).

19. Li, Y. *et al.* Optically Transparent Wood Substrate for Perovskite Solar Cells Optically Transparent Wood Substrate for Perovskite Solar Cells. (2019) doi:10.1021/acssuschemeng.8b06248.

20. Meng, L., You, J., Guo, T. & Yang, Y. Recent Advances in the Inverted Planar Structure of Perovskite Solar Cells. (2015) doi:10.1021/acs.accounts.5b00404.

21. Liu, T., Chen, K., Hu, Q., Zhu, R. & Gong, Q. Inverted Perovskite Solar Cells : Progresses and Perspectives. (2016) doi:10.1002/aenm.201600457.

22. Vivo, P., Salunke, J. K. & Priimagi, A. Hole-Transporting Materials for Printable Perovskite Solar Cells. 1–45 (2017) doi:10.3390/ma10091087.

23. Yu, Z. & Sun, L. Recent Progress on Hole-Transporting Materials for Emerging Organometal Halide Perovskite Solar Cells. (2015) doi:10.1002/aenm.201500213.

24. Chueh, C., Li, C. & Jen, A. K. Environmental Science Recent progress and perspective in solution-processed Interfacial materials for e ffi cient and stable polymer and organometal perovskite solar cells. 1160–1189 (2015) doi:10.1039/c4ee03824j.

25. Sajid, S. *et al.* Breakthroughs in NiOx-HTMs towards stable, low-cost and efficient perovskite solar cells. *Nano Energy* **51**, 408–424 (2018).

26. Yin, X., Guo, Y., Xie, H., Que, W. & Kong, L. B. Nickel Oxide as Efficient Hole Transport Materials for Perovskite Solar Cells. *Solar RRL* **3**, 1–27 (2019).

27. Pinar, F. *et al.* First demonstration of lithium , cobalt and magnesium introduced nickel oxide hole transporters for inverted methylammonium lead triiodide based perovskite solar cells. *Solar Energy* **215**, 434–442 (2021).

28. Nandy, S., Maiti, U. N., Ghosh, C. K. & Chattopadhyay, K. K. Enhanced p-type conductivity and band gap narrowing in heavily Al doped NiO thin films deposited by RF magnetron sputtering. *Journal of Physics Condensed Matter* **21**, (2009).

29. Azens, A., Kullman, L., Vaivars, G., Nordborg, H. & Granqvist, C. G. Sputter-deposited nickel oxide for electrochromic applications. *Solid State Ionics* **113–115**, 449–456 (1998).

30. Huran, J. & Spiess, L. Preparation and characterization of NiO thin " lms for gas. **58**, 300–307 (2000).

31. Shin, W. & Murayama, N. High performance p-type thermoelectric oxide based on NiO. *Materials Letters* **45**, 302–306 (2000).

32. Niu, G., Wang, S., Li, J., Li, W. & Wang, L. Oxygen doping in nickel oxide for highly efficient planar perovskite solar cells. *Journal of Materials Chemistry A* **6**, 4721–4728 (2018).

33. Sajid, S. *et al.* Breakthroughs in NiOx-HTMs towards stable, low-cost and efficient perovskite solar cells. *Nano Energy* **51**, 408–424 (2018).

34. di Girolamo, D. *et al.* Progress, highlights and perspectives on NiO in perovskite photovoltaics. *Chemical Science* **11**, 7746–7759 (2020).

35. Chen, P. C. & Yang, S. H. Potassium-Doped Nickel Oxide as the Hole Transport Layer for Efficient and Stable Inverted Perovskite Solar Cells. *ACS Applied Energy Materials* **2**, 6705–6713 (2019).

36. Jung, J. W., Chueh, C. C. & Jen, A. K. Y. A Low-Temperature, Solution-Processable, Cu-Doped Nickel Oxide Hole-Transporting Layer via the Combustion Method for High-Performance Thin-Film Perovskite Solar Cells. *Advanced Materials* **27**, 7874–7880 (2015).

37. Wei, Y. *et al.* Improving the efficiency and environmental stability of inverted planar perovskite solar cells via silver-doped nickel oxide hole-transporting layer. *Applied Surface Science* **427**, 782–790 (2018).

38. Wang, S. *et al.* Achieving high performance and stable inverted planar perovskite solar cells using lithium and cobalt co-doped nickel oxide as hole transport layers. *Journal of Materials Chemistry C* **7**, 9270–9277 (2019).

39. Wan, X. *et al.* Zinc as a New Dopant for NiOx-Based Planar Perovskite Solar Cells with Stable Efficiency near 20%. *ACS Applied Energy Materials* **1**, 3947–3954 (2018).

40. Chen, W. *et al.* Molecule-Doped Nickel Oxide: Verified Charge Transfer and Planar Inverted Mixed Cation Perovskite Solar Cell. *Advanced Materials* **30**, 1–9 (2018).

41. Wang, T. *et al.* Efficient Inverted Planar Perovskite Solar Cells Using Ultraviolet/Ozone-Treated NiOx as the Hole Transport Layer. *Solar RRL* **3**, 1–12 (2019).

42. Kim, J. *et al.* Effects of UV-ozone irradiation on copper doped nickel acetate and its applicability to perovskite solar cells. *Nanoscale* **8**, 9284–9292 (2016).

43. Wang, K., Tian, Y., Jiang, H., Chen, M. & Xu, S. Surface Treatment on Nickel Oxide to Enhance the Efficiency of Inverted Perovskite Solar Cells. *International Journal of Photoenergy* **2019**, (2019).

44. Li, G. *et al.* Overcoming the Limitations of Sputtered Nickel Oxide for High-Efficiency and Large-Area Perovskite Solar Cells. *Advanced Science* **4**, 1–8 (2017).

45. Chen, W. *et al.* Efficient and stable large-area perovskite solar cells with inorganic charge extraction layers. *Science* **350**, 944–948 (2015).

46. Lee, P. H. *et al.* High-efficiency perovskite solar cell using cobalt doped nickel oxide hole transport layer fabricated by NIR process. *Solar Energy Materials and Solar Cells* **208**, 110352 (2020).

47. Huang, A. B. *et al.* Achieving high-performance planar perovskite solar cells with co-sputtered Co-doping NiOx hole transport layers by efficient extraction and enhanced mobility. *Journal of Materials Chemistry C* **4**, 10839–10846 (2016).

48. Lee, J. H., Noh, Y. W., Jin, I. S., Park, S. H. & Jung, J. W. A solution-processed cobalt-doped nickel oxide for high e ffi ciency inverted type perovskite solar cells. *Journal of Power Sources* **412**, 425–432 (2019).

49. Kaneko, R. *et al.* Cobalt-doped nickel oxide nanoparticles as efficient hole transport materials for low-temperature processed perovskite solar cells. *Solar Energy* **181**, 243–250 (2019).

50. Zhang, K. H. L., Xi, K., Blamire, M. G. & Egdell, R. G. P -type transparent conducting oxides. *Journal of Physics: Condensed Matter* **383002**, 383002.

51. Banai, R. E. *et al.* Optical Properties of Sputtered SnS Thin Films for Photovoltaic Absorbers. **3**, 1084–1089 (2013).

52. Makuła, P., Pacia, M. & Macyk, W. How To Correctly Determine the Band Gap Energy of Modified Semiconductor Photocatalysts Based on UV-Vis Spectra. *Journal of Physical Chemistry Letters* **9**, 6814–6817 (2018).

53. Tyagi, M., Tomar, M. & Gupta, V. Postdeposition annealing of NiOx thin films: A transition from n-type to p-type conductivity for short wave length optoelectronic devices. *Journal of Materials Research* **28**, 723–732 (2013).

54. Wang, K. *et al.* Low-Temperature Sputtered Nickel Oxide Compact Thin Film as. *ACS applied materials & interfaces* **6**, 11851−11858 (2014).

55. Lin, Y. R., Liao, Y. S., Hsiao, H. T. & Chen, C. P. Two-step annealing of NiOx enhances the NiOx–perovskite interface for high-performance ambient-stable p–i–n perovskite solar cells. *Applied Surface Science* **504**, 144478 (2020).

56. Tailor, N. K. *et al.* Recent progress in morphology optimization in perovskite solar cell. *Journal of Materials Chemistry A* (2020) doi:10.1039/d0ta00143k.

57. Bishnoi, A., Kumar, S. & Joshi, N. *Chapter 9 - Wide-Angle X-ray Diffraction (WXRD): Technique for Characterization of Nanomaterials and Polymer Nanocomposites*. *Microscopy Methods in Nanomaterials Characterization* (Elsevier Inc., 2017). doi:10.1016/B978-0-323-46141-2.00009-2.

58. Monshi, A., Foroughi, M. R. & Monshi, M. R. Modified Scherrer Equation to Estimate More Accurately Nano-Crystallite Size Using XRD. **2012**, 154–160 (2012).

59. Marand, Z. R. *et al.* Structural and Electrical Investigation of Cobalt-Doped NiO x / Perovskite Interface for E ffi cient Inverted Solar Cells. 1–13 (2020).

60. Paquin, F., Rivnay, J., Salleo, A., Stingelin, N. & Silva, C. Multi-phase semicrystalline microstructures drive exciton dissociation in neat plastic semiconductors. *J. Mater. Chem. C* **3**, 10715–10722 (2015).

61. Li, G. *et al.* Overcoming the Limitations of Sputtered Nickel Oxide for High-Efficiency and Large-Area Perovskite Solar Cells. *Advanced Science* **4**, 1–8 (2017).

62. Wang, T. *et al.* Environmental Science methylammonium lead halide perovskite †. 509–515 (2017) doi:10.1039/c6ee03474h.

63. Hutter, E. M. *et al.* methylammonium lead iodide perovskite. **16**, (2017).

64. Park, N. G. Perovskite solar cells: An emerging photovoltaic technology. *Materials Today* **18**, 65–72 (2015).

65. K, R. D. *et al.* Rapid assessment of photovoltaic activity of perovskite solar cells by photoluminescence spectroscopy. *Materials Letters* **299**, 130056 (2021).

66. Lee, J. H., Noh, Y. W., Jin, I. S., Park, S. H. & Jung, J. W. Efficient perovskite solar cells with negligible hysteresis achieved by sol-gel-driven spinel nickel cobalt oxide thin films as the hole transport layer. *Journal of Materials Chemistry C* **7**, 7288–7298 (2019).

67. Wu, Y. *et al.* Perovskite solar cells with 18.21% efficiency and area over 1 cm2 fabricated by heterojunction engineering. *Nature Energy* **1**, 1–7 (2016).

68. Lee, K. *et al.* Enhanced efficiency and air-stability of NiO:X-based perovskite solar cells via PCBM electron transport layer modification with Triton X-100. *Nanoscale* **9**, 16249–16255 (2017).

69. Liu, X. *et al.* Enhancement of the efficiency and stability of planar p-i-n perovskite solar cells via incorporation of an amine-modified fullerene derivative as a cathode buffer layer. *Science China Chemistry* **60**, 136–143 (2017).

70. Guo, X. *et al.* intermediate phase in hybrid organic – inorganic. (2016) doi:10.1039/c5dt04420k.

71. Brunetti, B., Cavallo, C., Ciccioli, A., Gigli, G. & Latini, A. On the Thermal and Thermodynamic (In) Stability of Methylammonium Lead Halide Perovskites. *Nature Publishing Group* 1–10 (2016) doi:10.1038/srep31896.

72. Park, N. G. Perovskite solar cells: An emerging photovoltaic technology. *Materials Today* **18**, 65–72 (2015).

73. Guo, X., Mccleese, C., Kolodziej, C. & Samia, A. C. S. Identification and Characterization of the Intermediate Phase in Hybrid Organic – Inorganic MAPbI 3 Perovskite. (2016).

74. Manuscript, A. Materials Advances. (2021) doi:10.1039/D1MA00432H.

75. Manjunath, V., Bimli, S., Parmar, K. H., Shirage, P. M. & Devan, R. S. Oxidized Nickel films as highly transparent HTLs for inverted planar perovskite solar cells. *Solar Energy* **193**, 387–394 (2019).

76. Chen, C. *et al.* Effect of BCP buffer layer on eliminating charge accumulation for high performance of inverted perovskite solar cells. *RSC Advances* **7**, 35819–35826 (2017).

77. Guo, X. *et al.* A 16.5% efficient perovskite solar cells with inorganic NiO film as hole transport material. *IEEE Journal of Photovoltaics* **8**, 1039–1043 (2018).

78. Guo, X. *et al.* A 16 . 5 % Efficient Perovskite Solar Cells With Inorganic NiO Film as Hole Transport Material. 1–5 (2018).

79. Tsai, H. *et al.* Light-induced lattice expansion leads to high-efficiency perovskite solar cells. **70**, 67–70 (2018).

80. Wenger, B. *et al.* Towards unification of perovskite stability and photovoltaic performance assessment. 1–9 (2020).

81. Zhao, C. *et al.* Revealing Underlying Processes Involved in Light Soaking Effects and Hysteresis Phenomena in Perovskite Solar Cells. *Advanced Energy Materials* **5**, 1–6 (2015).

82. Deng, X. *et al.* Dynamic study of the light soaking effect on perovskite solar cells by in-situ photoluminescence microscopy. *Nano Energy* **46**, 356–364 (2018).

83. He, Q. *et al.* Room-Temperature and Solution-Processable Cu-Doped Nickel Oxide Nanoparticles for Efficient Hole-Transport Layers of Flexible Large-Area Perovskite Solar Cells Room-Temperature Solution-Processable Cu-Doped Abstract : (2017) doi:10.1021/acsami.7b13621.

84. Cong, S. *et al.* Fabrication of Nickel Oxide Nanopillar Arrays on Flexible Electrodes for Highly Efficient Perovskite Solar Cells. *Nano Letters* **19**, 3676–3683 (2019).

85. Zhu, Z. *et al.* Metal halide perovskites: stability and sensing-ability. *Journal of Materials Chemistry C* **6**, 10121–10137 (2018).

Appendices

A. Solar Simulation Parameters

In this section, it will be explained how the solar cell parameters are calculated. Using electrical characterization we obtain the JV curve, a generic example is demonstrated in Figure 20, alongside with the equations presented bellow, we generate the solar cell parameters.

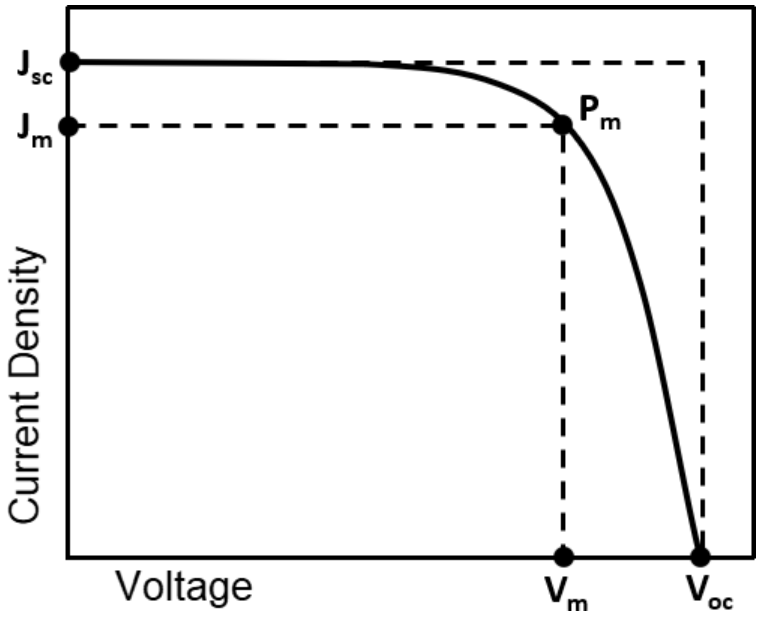

Figure 20 - Representation of solar cell parameters on a generic JV curve.

J_{sc} (short circuit current density) is the current density value for V = 0 V;

V_{oc} (open circuit voltage) is the voltage value for J = 0 A/m^2;

J_m and V_m are the maximum current and voltage, respectively, and can be interpreted by analysing the JV curve;

P_{max} (maximum power):$P_{max}= Jm\ x\ Vm\ x\ P_{max}$ (9)

FF (fill factor), approximation of the J-V curve to a square:

$$FF = \frac{Jm\ x\ Vm}{Jsc\ x\ Voc} \qquad (10)$$

PCE (Power conversion efficiency), ratio between Pmax and Plight (light power = 1000 W/m^2):

$$PCE(\%) = \frac{Pmax}{Plight}\ x\ 100 \qquad (11)$$

B. Substrate Preparation

The device fabrication begins by cutting ITO (2.5 x 2.5 cm), after that these substrates go through a cleaning procedure. This procedure begins by cleaning the substrates supports and recipients with DI water for 10 minutes in sonication bath. Then the substrates are place into sonication bath for 35 minutes with a temperature of 35 ºC while submerged with DI Water with 1% concentration of Hellmnex detergent solution. Followed by 2 steps of 15 minutes each, sonication bath with just DI water (an additional third step might be needed if the detergent solution is not properly removed). Then the substrates are dried with N2 gas, before being put back into sonication bath for 15 minutes this time using acetone and after that another sonication bath, for 15 minutes, is conducted with isopropanol (IPA) at room temperature. After drying, with N2 gun, the substrates must be cleaned and look spotless.

C. Materials

Table 8 - List of reagents, with their respective abbreviation, purity, company and CAS referance.

Compound	***Abbreviation***	***Purity***	***Company***	***CAS***
Ethanol Absolute	EtOH	99.99 %	Fisher Chemical	64-17-5
Bathocuproine	BCP	96 %	Sigma-Aldrich	4733-39-5
Chlorobenzene	CB	≥99.9 %	Honeywell	108-90-7
Chloroform	CF	99.8%	Fisher	67-66-3
Cobalt (II) acetate	-	99.999%	Sigma-Aldrich	6147-53-1
1,2-Dichlorobenzene	DCB	99%	Sigma-Aldrich	95-50-1
Ethanolamine	MEA	≥99.5%	Sigma-Aldrich	141-43-5
2-Propanol	IPA	99.8%	Sigma-Aldrich	67-63-0
γ-Butyrolactone	GBL	≥ 99 %	Sigma-Aldrich	96-48-0
Lead (II) Iodide	PbI_2	99.999	Sigma-Aldrich	10101-63-0
Magnesium Acetate	-	-	Sigma-Aldrich	16674-78-5
Methylammonium Iodide	MAI	98 %	Sigma-Aldrich	14965-49-2
Nickel Acetate tetrahydrate	-	98%	Sigma-Aldrich	6018-89-9
[6,6]-Phenyl-C61-butyric	PCBM	≥ 99 %	Ossila	160848-22-6
Toluene	-	-	Carlo Erba	108-88-3

D. Solution Preparation

HTL precursor solution

For the control group (undoped Nickel oxide), 125 mg of Nickel Acetate tetrahydrate were dissolved in 5ml IPA solution and 30 µl MEA.

For the cobalt doped Nickel oxide 125 mg of Nickel Acetate tetrahydrate and 7.2 mg of Cobalt(II) acetate tetrahydrate were dissolved in 5ml IPA and 30 µl MEA solution.

For the Magnesium doped Nickel oxide 125 mg of Nickel Acetate tetrahydrate and 6.4 mg of Magnesium Acetate tetrahydrate were dissolved in 5ml IPA and 30 µl MEA solution.

For the Magnesium and Cobalt doped Nickel oxide 125 mg of Nickel Acetate tetrahydrate, 6.4 mg of magnesium acetate tetrahydrate and 7.2 mg of Cobalt(II) acetate tetrahydrate were dissolved in 5ml IPA and 30 µl MEA solution.

The solutions described above went stirring at 85ºC for 4 hours, which means that the solution preparation must take 4 hour prior to the deposition.

Perovskite precursor solution

Solution 1:

- $MAPbI_3$ in GBL (1 ml) 1.2 mmol: 1.2 mmol (PbI2/MAI)

Solution 2:

- $MAPbI_3$ in (GBL+ DMF + DMSO) (4:3:3) 1.2 mmol: 1.2 mmol (PbI2/MAI)

Solution 3:

- $MAPbI_3$ in (DMF + DMSO) (7:3) 1.2 mmol: 1.2 mmol (PbI2/MAI)

The solutions were then placed stirring at 1000 rpm in a hot plate at 70 ºC overnight. Before the deposition the solution is filtered with PTFE filters with 0.22 µm grading

ETL solution

The electron transport layer precursor solution was prepared by dissolving PCBM powder with a concentration of 20 mg of PCBM for 0.5 mL of chlorobenzene and 0.5 mL of dichlorobenzene mixture.

Buffer Layer Solution

The buffer layer solution was obtained by dissolving BCP powder in absolute ethanol, with a concentration of 0.5 mg/mL.

E. UV-VIS-NIR data of HTLs

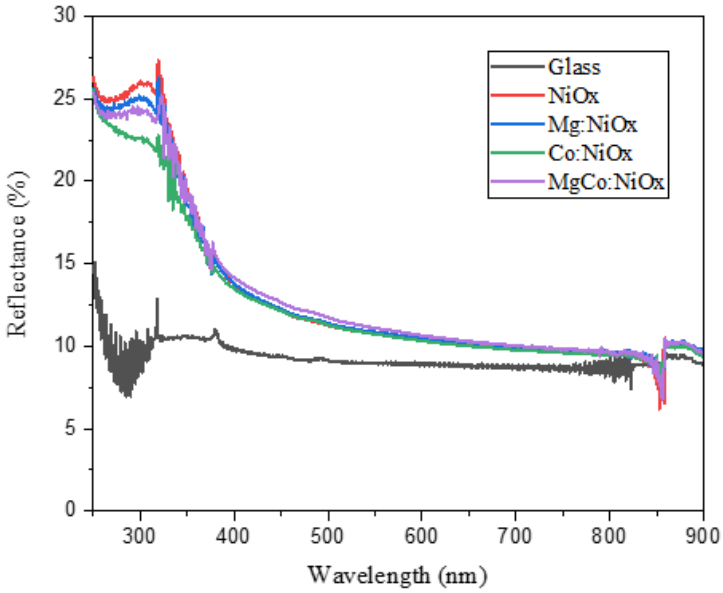

Figure 21 - Reflectance plot of NiO_x samples deposited on glass.

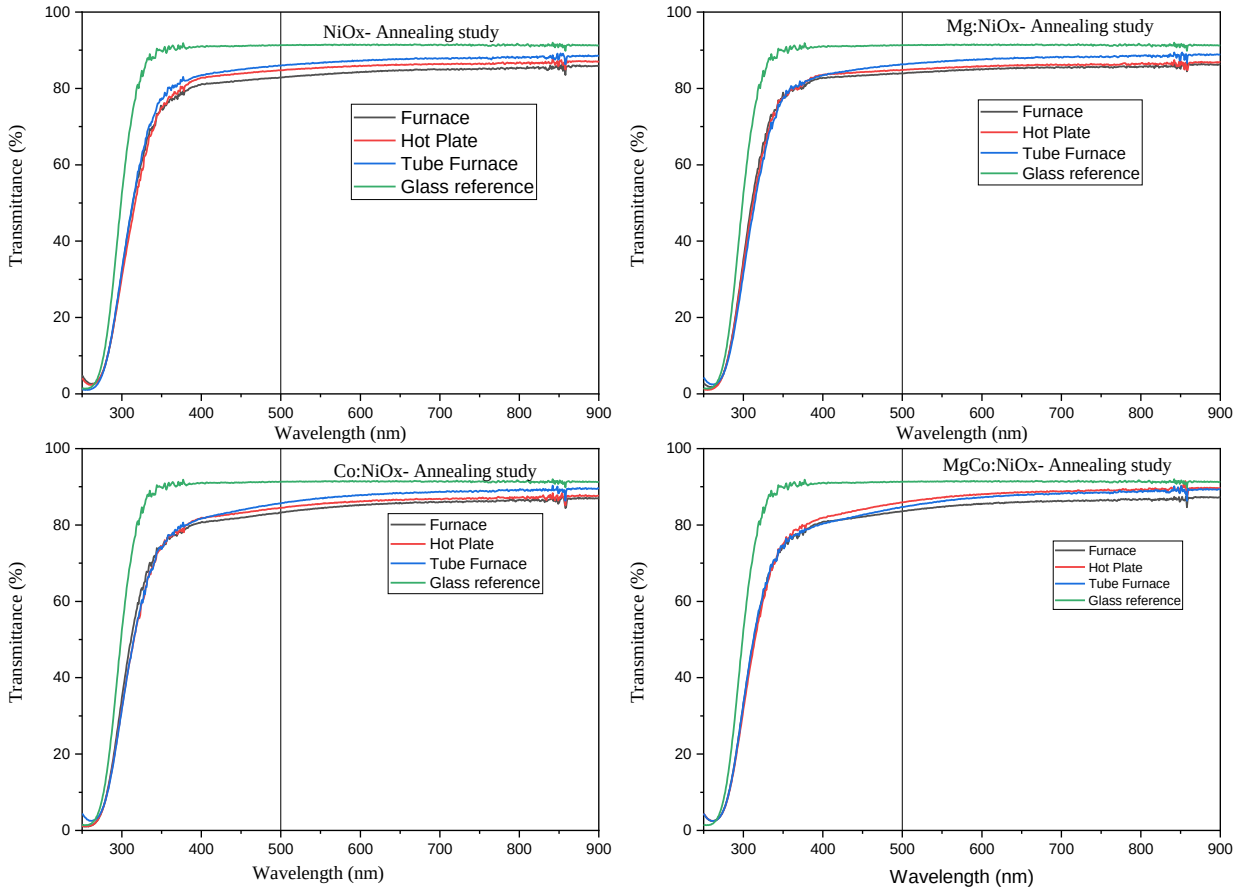

Figure 22 - Transmittance data regarding the four different HTLs using three different annealing equipments: furnace, hot plate and tube furnace.

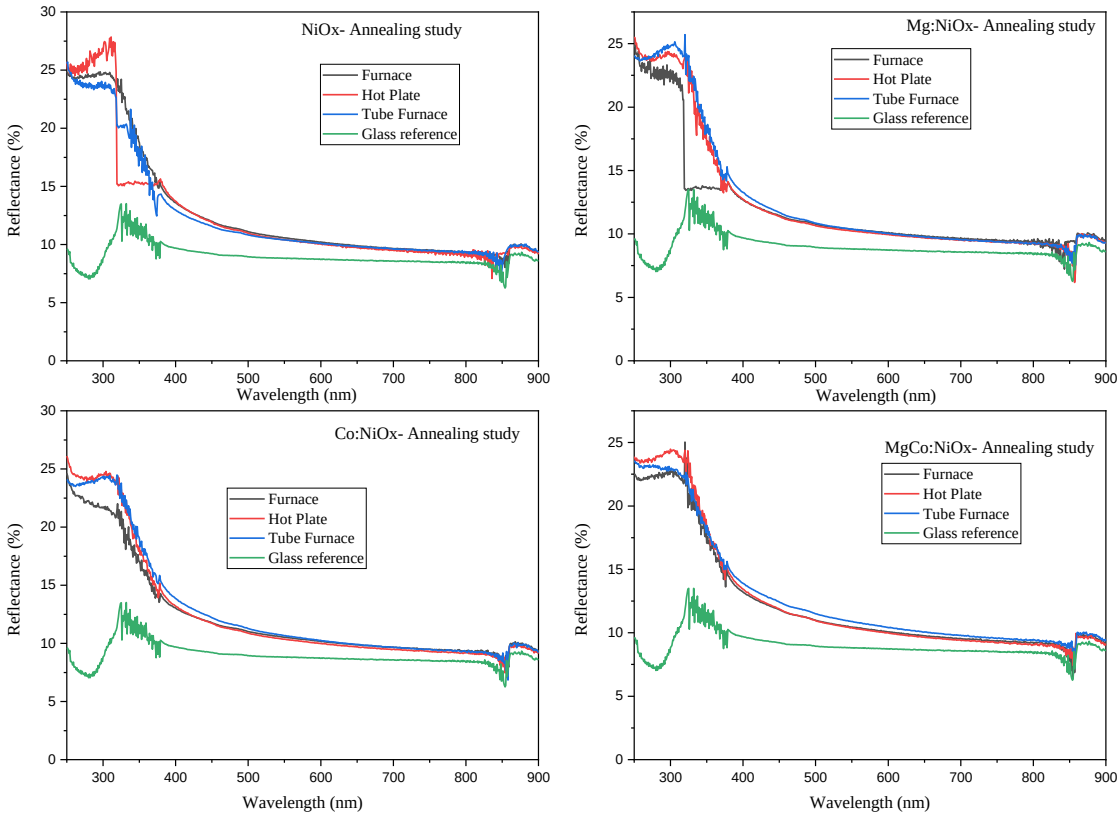

Figure 23 - Reflectance data regarding the four different HTLs using three different annealing equipments: furnace, hot plate and tube furnace.

F. Aditional topographical measurements

Table 9 - RMS value of the four different HTLs, obtained via AFM, deposited either on ITO or FTO coated glass substrates.

NiO_x Sample	*Average RMS (nm)*	
	ITO	*FTO*
substrates	1.929	37.89
Pristine NiO_x	1.808	10.2
Magnesium - doped NiO_x	1.572	9.447
Cobalt - doped NiO_x	1.670	9.304
Co - doped NiO_x	1.791	9.033

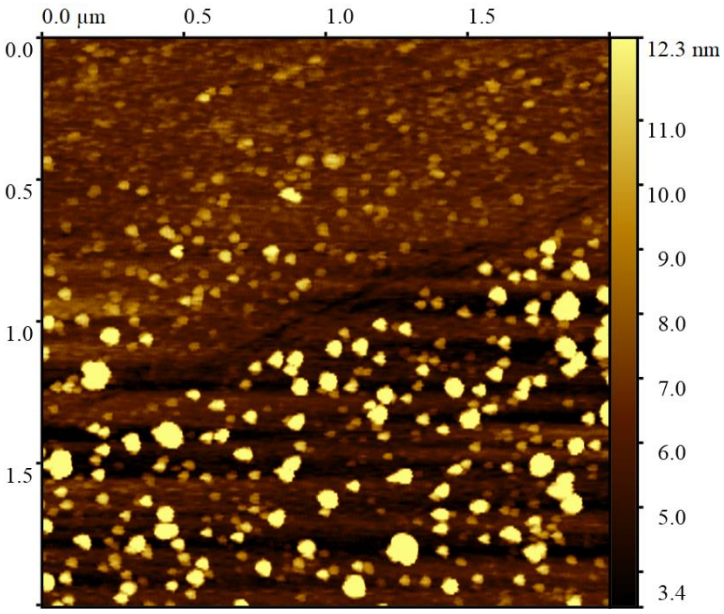

Figure 24 - AFM topographical images of glass substrate, obtained by Gwyddion software, with a RMS value of 2.728 nm.

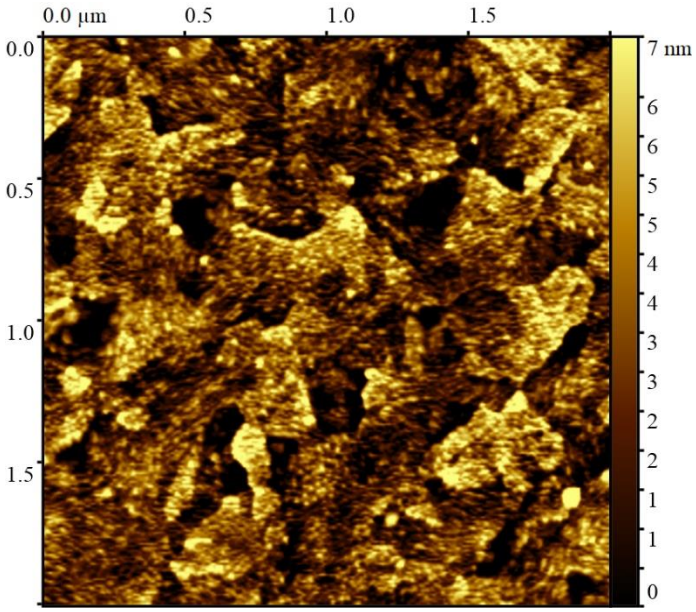

Figure 25 - AFM topographical images of glass coated ITO, obtained by Gwyddion software, with a RMS value of 1.929 nm.

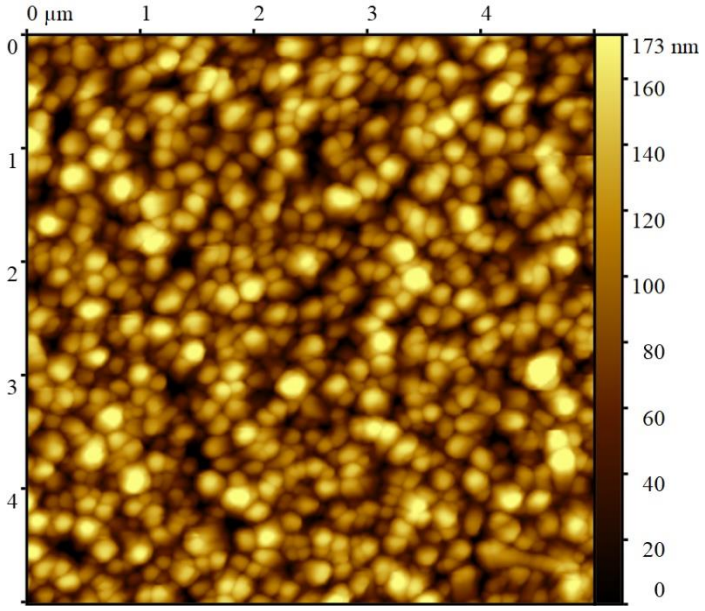

Figure 26 - AFM topographical images of glass coated FTO, obtained by Gwyddion software, with a RMS value of 37.89 nm.

G. Perovskite characterization

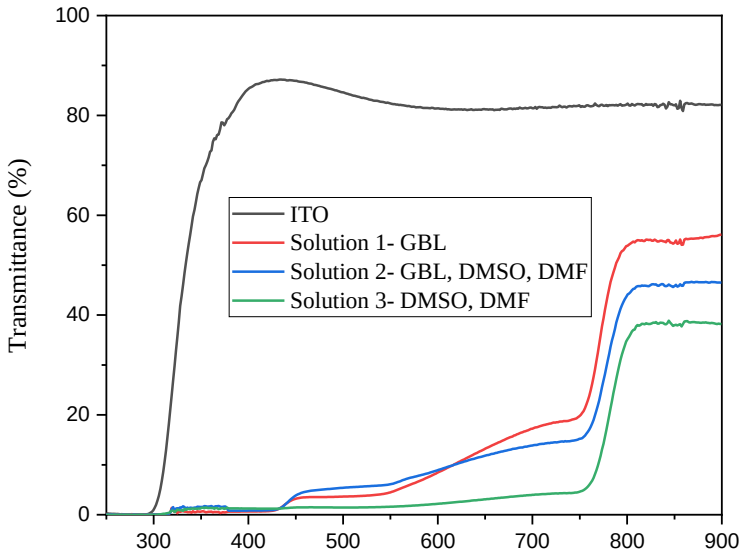

Figure 27 - Transmittance of $MAPbI_3$ perovskite films.

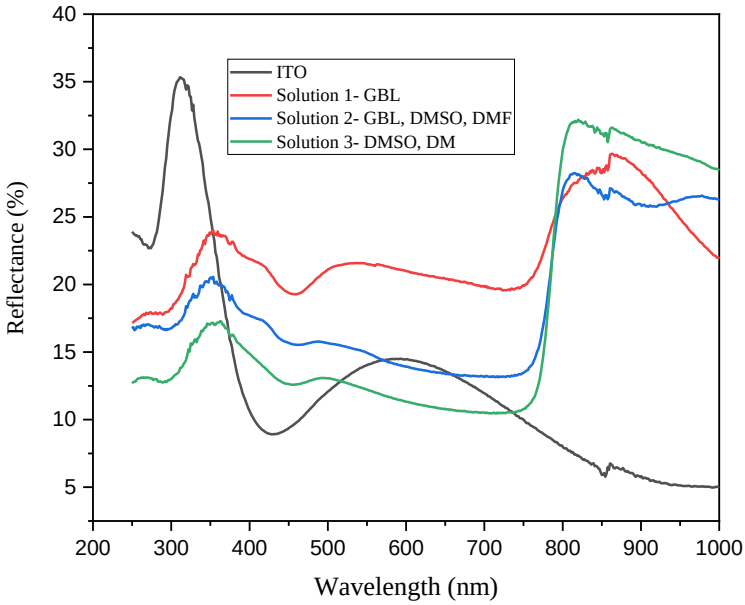

Figure 28 - Reflectance of $MAPbI_3$ perovskite films.

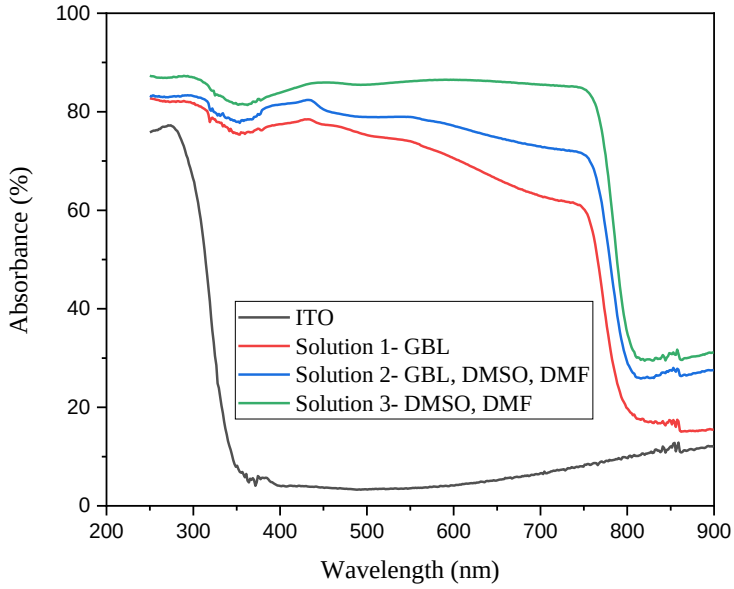

Figure 29 - Absorbance of $MAPbI_3$ perovskite films.

H. Supplementary Figures

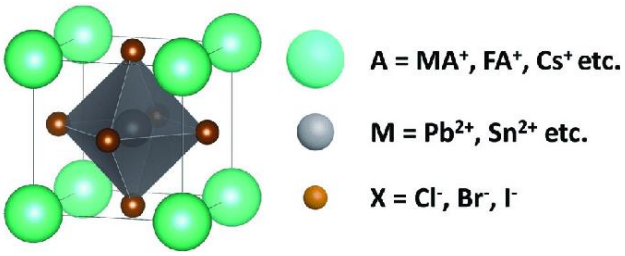

Figure 30 - Cubic crystal structure of an AMX_3 perovskite with common substituents listed for the A, M, and X positions[85].

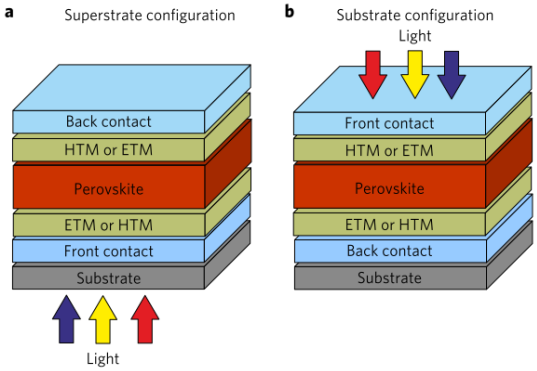

Figure 31- Schematic of a perovskite solar cell in the a) conventional superstrate configuration and b) substrate configuration[15]

I. Annealing Equipment

Figure 32- Picture of the Nabertherm furnace used to anneal NiO_x.

Figure 33- Picture of tube furnace used to anneal NiO_x.

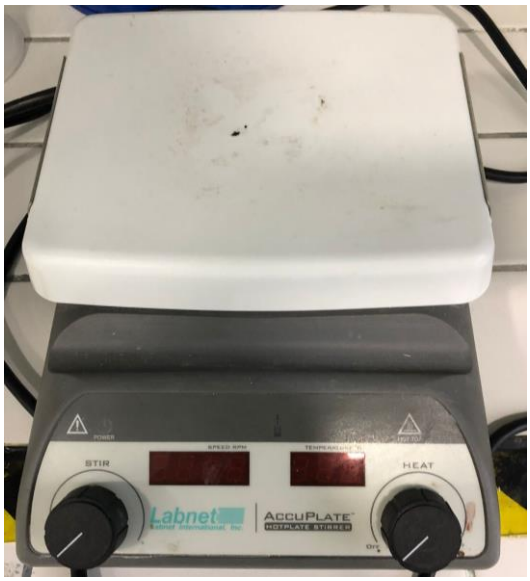

Figure 34- Picture of hot plate used to anneal NiO_x and perovskite layers.

NOVA SCHOOL OF SCIENCE & TECHNOLOGY

Solution Processed NiO_x as a Hole Transporting Layer for Inverted Perovskite solar Cells

André Morujo Ramos

2021